

# Hadronic Shower Development in Iron-Scintillator Tile Calorimetry

*Submitted to Nucl. Instr. & Meth.*

P. Amaral<sup>k1,k2</sup>, A. Amorim<sup>k1,k2</sup>, K. Anderson<sup>f</sup>, G. Barreira<sup>k1</sup>, R. Benetta<sup>j</sup>, S. Berglund<sup>r</sup>,  
C. Biscarat<sup>g</sup>, G. Blanchot<sup>c</sup>, E. Blucher<sup>f</sup>, A. Bogush<sup>l</sup>, C. Boehm<sup>r</sup>, V. Boldea<sup>e</sup>, O. Borisov<sup>h</sup>,  
M. Bosman<sup>c</sup>, C. Bromberg<sup>i</sup>, J. Budagov<sup>h</sup>, S. Burdin<sup>m</sup>, L. Caloba<sup>q</sup>, J. Carvalho<sup>k3</sup>,  
P. Casado<sup>c</sup>, M. V. Castillo<sup>t</sup>, M. Cavalli-Sforza<sup>c</sup>, V. Cavasinni<sup>m</sup>, R. Chadelas<sup>g</sup>,  
I. Chirikov-Zorin<sup>h</sup>, G. Chlachidze<sup>h</sup>, M. Cobal<sup>j</sup>, F. Cogswell<sup>s</sup>, F. Colaço<sup>k4</sup>, S. Cologna<sup>m</sup>,  
S. Constantinescu<sup>e</sup>, D. Costanzo<sup>m</sup>, M. Crouau<sup>g</sup>, F. Daudon<sup>g</sup>, J. David<sup>p</sup>, M. David<sup>k1,k2</sup>,  
T. Davidek<sup>n</sup>, J. Dawson<sup>a</sup>, K. De<sup>b</sup>, T. Del Prete<sup>m</sup>, A. De Santo<sup>m</sup>, B. Di Girolamo<sup>m</sup>,  
S. Dita<sup>e</sup>, J. Dolejsi<sup>n</sup>, Z. Dolezal<sup>n</sup>, R. Downing<sup>s</sup>, I. Efthymiopoulos<sup>c</sup>, M. Engström<sup>r</sup>,  
D. Errede<sup>s</sup>, S. Errede<sup>s</sup>, H. Evans<sup>f</sup>, A. Fenyuk<sup>p</sup>, A. Ferrer<sup>t</sup>, V. Flaminio<sup>m</sup>, E. Gallas<sup>b</sup>,  
M. Gaspar<sup>q</sup>, I. Gil<sup>t</sup>, O. Gildemeister<sup>j</sup>, V. Glagolev<sup>h</sup>, A. Gomes<sup>k1,k2</sup>, V. Gonzalez<sup>t</sup>,  
S. González De La Hoz<sup>t</sup>, V. Grabski<sup>u</sup>, E. Grauges<sup>c</sup>, P. Grenier<sup>g</sup>, H. Hakopian<sup>u</sup>, M. Haney<sup>s</sup>,  
M. Hansen<sup>j</sup>, S. Hellman<sup>r</sup>, A. Henriques<sup>k1</sup>, C. Hebrard<sup>g</sup>, E. Higon<sup>t</sup>, S. Holmgren<sup>r</sup>,  
J. Huston<sup>i</sup>, Yu. Ivanyushenkov<sup>c</sup>, K. Jon-And<sup>r</sup>, A. Juste<sup>c</sup>, S. Kakurin<sup>h</sup>, G. Karapetian<sup>j</sup>,  
A. Karyukhin<sup>p</sup>, S. Kopikov<sup>p</sup>, V. Kukhtin<sup>h</sup>, Y. Kulchitsky<sup>l,h</sup>, W. Kurzbauer<sup>j</sup>, M. Kuzmin<sup>l</sup>,  
S. Lami<sup>m</sup>, V. Lapin<sup>p</sup>, C. Lazzeroni<sup>m</sup>, A. Lebedev<sup>h</sup>, R. Leitner<sup>n</sup>, J. Li<sup>b</sup>, Yu. Lomakin<sup>h</sup>,  
O. Lomakina<sup>h</sup>, M. Lokajicek<sup>o</sup>, J. M. Lopez Amengual<sup>t</sup>, A. Maio<sup>k1,k2</sup>, S. Malyukov<sup>h</sup>,  
F. Marroquin<sup>q</sup>, J. P. Martins<sup>k1,k2</sup>, E. Mazzoni<sup>m</sup>, F. Merritt<sup>f</sup>, R. Miller<sup>i</sup>, I. Minashvili<sup>h</sup>,  
Ll. Miralles<sup>c</sup>, G. Montarou<sup>g</sup>, A. Munar<sup>t</sup>, S. Nemecek<sup>o</sup>, M. Nessi<sup>j</sup>, A. Onofre<sup>k3,k4</sup>, S. Orteu<sup>c</sup>,  
I.C. Park<sup>c</sup>, D. Pallin<sup>g</sup>, D. Pantea<sup>d,h</sup>, R. Paoletti<sup>m</sup>, J. Patriarca<sup>k1</sup>, A. Pereira<sup>q</sup>, J. A. Perlas<sup>c</sup>,  
P. Petit<sup>c</sup>, J. Pilcher<sup>f</sup>, J. Pinhão<sup>k3</sup>, L. Poggioli<sup>j</sup>, L. Price<sup>a</sup>, J. Proudfoot<sup>a</sup>, O. Pukhov<sup>h</sup>,  
G. Reinmuth<sup>g</sup>, G. Renzoni<sup>m</sup>, R. Richards<sup>i</sup>, C. Roda<sup>m</sup>, J. B. Romance<sup>t</sup>, V. Romanov<sup>h</sup>,  
B. Ronceux<sup>c</sup>, P. Rosnet<sup>g</sup>, V. Rumyantsev<sup>l,h</sup>, N. Russakovich<sup>h</sup>, E. Sanchis<sup>t</sup>, H. Sanders<sup>f</sup>,  
C. Santoni<sup>g</sup>, J. Santos<sup>k1</sup>, L. Sawyer<sup>b</sup>, L.-P. Says<sup>g</sup>, J. M. Seixas<sup>q</sup>, B. Selldèn<sup>r</sup>, A. Semenov<sup>h</sup>,  
A. Shchelchkov<sup>h</sup>, M. Shochet<sup>f</sup>, V. Simaitis<sup>s</sup>, A. Sissakian<sup>h</sup>, A. Solodkov<sup>p</sup>, O. Solovianov<sup>p</sup>,  
P. Sonderegger<sup>j</sup>, M. Sosebee<sup>b</sup>, K. Soustruznik<sup>n</sup>, F. Spanó<sup>m</sup>, R. Stanek<sup>a</sup>, E. Starchenko<sup>p</sup>,  
R. Stephens<sup>b</sup>, M. Suk<sup>n</sup>, F. Tang<sup>f</sup>, P. Tas<sup>n</sup>, J. Thaler<sup>s</sup>, S. Tokar<sup>d</sup>, N. Topilin<sup>h</sup>, Z. Trka<sup>n</sup>,  
A. Turcot<sup>f</sup>, M. Turcotte<sup>b</sup>, S. Valkar<sup>n</sup>, M. J. Varandas<sup>k1,k2</sup>, A. Vartapetian<sup>u</sup>, F. Vazeille<sup>g</sup>,  
I. Vichou<sup>c</sup>, V. Vinogradov<sup>h</sup>, S. Vorozhtsov<sup>h</sup>, D. Wagner<sup>f</sup>, A. White<sup>b</sup>, H. Wolters<sup>k4</sup>,  
N. Yamdagni<sup>r</sup>, G. Yarygin<sup>h</sup>, C. Yosefi<sup>i</sup>, A. Zaitsev<sup>p</sup>, M. Zdrazil<sup>n</sup>, J. Zuñiga<sup>t</sup>

- <sup>a</sup> *Argonne National Laboratory, Argonne, Illinois, USA*
- <sup>b</sup> *University of Texas at Arlington, Arlington, Texas, USA*
- <sup>c</sup> *Institut de Fisica d'Altes Energies, Universitat Autònoma de Barcelona, Barcelona, Spain*
- <sup>d</sup> *Comenius University, Bratislava, Slovakia*
- <sup>e</sup> *Institute of Atomic Physics, Bucharest, Rumania*
- <sup>f</sup> *University of Chicago, Chicago, Illinois, USA*
- <sup>g</sup> *LPC Clermont–Ferrand, Université Blaise Pascal / CNRS–IN2P3, Clermont–Ferrand, France*
- <sup>h</sup> *JINR, Dubna, Russia*
- <sup>i</sup> *Michigan State University, East Lansing, Michigan, USA*
- <sup>j</sup> *CERN, Geneva, Switzerland*
- <sup>k</sup> *1) LIP Lisbon, 2) FCUL Univ. of Lisbon, 3) LIP and FCTUC Univ. of Coimbra, 4) Univ. Católica Figueira da Foz, Portugal*
- <sup>l</sup> *Institute of Physics, National Academy of Science, Minsk, Republic of Belarus*
- <sup>m</sup> *Pisa University and INFN, Pisa, Italy*
- <sup>n</sup> *Charles University, Prague, Czech Republic*
- <sup>o</sup> *Academy of Science, Prague, Czech Republic*
- <sup>p</sup> *Institute for High Energy Physics, Protvino, Russia*
- <sup>q</sup> *COPPE/EE/UFRJ, Rio de Janeiro, Brazil*
- <sup>r</sup> *Stockholm University, Stockholm, Sweden*
- <sup>s</sup> *University of Illinois, Urbana–Champaign, Illinois, USA*
- <sup>t</sup> *IFIC, Centro Mixto Universidad de Valencia-CSIC, E46100 Burjassot, Valencia, Spain*
- <sup>u</sup> *Yerevan Physics Institute, Yerevan, Armenia*

## **Abstract**

The lateral and longitudinal profiles of hadronic showers detected by a prototype of the ATLAS Iron-Scintillator Tile Hadron Calorimeter have been investigated. This calorimeter uses a unique longitudinal configuration of scintillator tiles. Using a fine-grained pion beam scan at 100 GeV, a detailed picture of transverse shower behavior is obtained. The underlying radial energy densities for four depth segments and for the entire calorimeter have been reconstructed. A three-dimensional hadronic shower parametrization has been developed. The results presented here are useful for understanding the performance of iron-scintillator calorimeters, for developing fast simulations of hadronic showers, for many calorimetry problems requiring the integration of a shower energy deposition in a volume and for future calorimeter design.

Keywords: Calorimetry; Computer data analysis.

# 1 Introduction

We report on an experimental study of hadronic shower profiles detected by the prototype of the ATLAS Barrel Tile Hadron Calorimeter (Tile calorimeter) [1], [2]. The innovative design of this calorimeter, using longitudinal segmentation of active and passive layers (see Fig. 1), provides an interesting system for the measurement of hadronic shower profiles. Specifically, we have studied the transverse development of hadronic showers using 100 GeV pion beams and longitudinal development of hadronic showers using 20 – 300 GeV pion beams.

Characteristics of shower development in hadron calorimeters have been published for some time. However, a complete quantitative description of transverse and longitudinal properties of hadronic showers does not exist [3]. The transverse profiles are usually expressed as a function of transverse coordinates, not the radius, and are integrated over the other coordinate [4]. The three-dimensional parametrization of hadronic showers described here could be a useful starting point for fast simulations, which can be faster than full simulations at the microscopic level by several orders of magnitude [5], [6], [7].

The paper is organised as follows. In Section 2, the calorimeter and the test beam setup are briefly described. In Section 3, the mathematical procedures for extracting the underlying radial energy density of hadronic showers are developed. The obtained results on the transverse and longitudinal profiles, the radial energy densities and the radial containment of hadronic shower are presented in Sections 4 – 7. Section 8 and 9 investigate the three-dimensional parametrization and electromagnetic fraction of hadronic shower. Finally Section 10 contains a summary and the conclusions.

## 2 The Calorimeter

The prototype Tile Calorimeter used for this study is composed of five modules stacked in the  $Y$  direction, as shown in Fig. 2. Each module spans  $2\pi/64$  in the azimuthal angle, 100 cm in the  $Z$  direction, 180 cm in the  $X$  direction (about 9 interaction lengths,  $\lambda_I$ , or about 80 effective radiation lengths,  $X_0$ ), and has a front face of  $100 \times 20 \text{ cm}^2$  [8]. The absorber structure of each module consists of 57 repeated “periods”. Each period is 18 mm thick and consists of four layers. The first and third layers are formed by large trapezoidal steel plates (master plates) and span the full longitudinal dimension of the module. In the second and fourth layers, smaller trapezoidal steel plates (spacer plates) and scintillator tiles alternate along the  $X$  direction. These layers consist of 18 different trapezoids of steel or scintillator, each of 100 mm in depth. The master plates, spacer plates and scintillator tiles are 5 mm, 4 mm and 3 mm thick, respectively. The iron to scintillator ratio is 4.67 : 1 by volume. The calorimeter thickness along the beam direction at the incidence angle (the angle between the incident particle direction and the normal to the calorimeter front face) of  $\Theta = 10^\circ$  corresponds to 1.49 m of iron equivalent [9].

Wavelength shifting fibers collect scintillation light from the tiles at both of their open (azimuthal) edges and bring it to photo-multipliers (PMTs) at the periphery of the calorimeter. Each PMT views a specific group of tiles through the corresponding bundle of fibers. The modules are divided into five segments along  $Z$ . They are also longitudinally segmented (along  $X$ ) into four depth segments. The readout cells have a lateral dimensions of 200 mm along  $Z$ , and longitudinal dimensions of 300, 400, 500, 600 mm for depth segments 1 – 4, corresponding to 1.5, 2, 2.5 and 3  $\lambda_I$  at  $\Theta = 0^\circ$  respectively. Along  $Y$ , the cell sizes vary between about 200 and 370 mm depending on the  $X$  (depth) coordinate. We recorded energies for 100 different cells for each event [8].

The calorimeter was placed on a scanning table that allowed movement in any direction.

Upstream of the calorimeter, a trigger counter telescope (S1 – S3) was installed, defining a beam spot approximately 20 mm in diameter. Two delay-line wire chambers (BC1 – BC2), each with ( $Z, Y$ ) readout, allowed the impact point of beam particles on the calorimeter face to be reconstructed to better than  $\pm 1$  mm [10]. “Muon walls” were placed behind ( $800 \times 800$  mm<sup>2</sup>) and on the positive  $Z$  side ( $400 \times 1150$  mm<sup>2</sup>) of the calorimeter modules to measure longitudinal and lateral hadronic shower leakage [11].

We used the TILEMON program [12] to convert the raw calorimeter data into PAW Ntuples [13] containing calibrated cell energies and other information used in this study.

The data used for the study of lateral profiles were collected in 1995 during a special  $Z$ -scan run at the CERN SPS test beam. The calorimeter was exposed to 100 GeV negative pions at a  $10^\circ$  angle with varying impact points in the  $Z$ -range from  $-360$  to  $+200$  mm. A total of  $> 300,000$  events have been analysed; for the lateral profile study only events without lateral leakage were used. The uniformity of the calorimeter’s response for this  $Z$ -scan is estimated to be 1% [14].

The data used for the study of longitudinal profiles were obtained using 20 – 300 GeV negative pions at a  $20^\circ$  angle and were also taken in 1995 during the same test beam run.

### 3 Extracting the Underlying Radial Energy Density

In this investigation we use a coordinate system based on the incident particle direction. The impact point of the incident particle at the calorimeter front face defines the origin of coordinate system. The incident particle direction forms the  $x$  axis, while the  $y$  axis is in the same direction as  $Y$  defined in Section 2. The normal to the  $xy$  surface defines the  $z$  axis.

We measure the energy deposition in each calorimeter cell for every event. In the  $ijk$ -cell of the calorimeter with the volume  $V_{ijk}$  and cell center coordinates  $(x_c, y_c, z_c)$ , the energy deposition  $E_{ijk}$  is

$$E_{ijk}(x_c, y_c, z_c) = \int_{V_{ijk}} f(x, y, z) dx dy dz, \quad (1)$$

where  $f(x, y, z)$  is the three-dimensional hadronic shower energy density function. Due to the azimuthal symmetry of shower profiles, the density  $f(x, y, z)$  is only a function of the radius  $r = \sqrt{y^2 + z^2}$  from the shower axis and the longitudinal coordinate  $x$ . Then

$$E_{ijk}(x_c, y_c, z_c) = \int_{V_{ijk}} \Psi(x, r) r dr d\phi dx, \quad (2)$$

where  $\phi$  is the azimuthal angle and  $\Psi(x, r)$  has the form of a joint probability density function (p.d.f.) [15]. The joint p.d.f. can be further decomposed as a product of the marginal p.d.f.,  $dE(x)/dx$ , and the conditional p.d.f.,  $\Phi(x, r)$ ,

$$\Psi(x, r) = \frac{dE(x)}{dx} \cdot \Phi(x, r). \quad (3)$$

The longitudinal density  $dE/dx$  is defined as

$$\frac{dE(x)}{dx} = \int_{-\infty}^{\infty} \int_{-\infty}^{\infty} f(x, y, z) dy dz. \quad (4)$$

Finally, the radial density function  $\Phi(r)$  for a given depth segment is

$$\Phi(r) = E_0 \Phi(x, r), \quad (5)$$

where  $E_0$  is the total shower energy deposition into the depth segment for fixed  $x$ .

There are several methods for extracting the radial density  $\Phi(r)$  from the measured distributions of energy depositions. One method is to unfold  $\Phi(r)$  using expression (2). This method was used in the analysis of the data from the lead-scintillating fiber calorimeter [16]. Several analytic forms of  $\Phi(r)$  were tried, but the simplest that describes the energy deposition in cells was a combination of an exponential and a Gaussian:

$$\Phi(r) = \frac{b_1}{r} e^{-\frac{r}{\mu_1}} + \frac{b_2}{r} e^{-\left(\frac{r}{\mu_2}\right)^2}, \quad (6)$$

where  $b_i$  and  $\mu_i$  are the free parameters.

Another method for extracting the radial density is to use the marginal density function

$$f(z) = \int_{-\infty}^{\infty} \int_{x_1}^{x_2} f(x, y, z) dx dy. \quad (7)$$

which is related to the radial density  $\Phi(r)$

$$f(z) = 2 \int_{|z|}^{\infty} \frac{\Phi(r) r dr}{\sqrt{r^2 - z^2}}. \quad (8)$$

This method was used [17] for extracting the electron shower transverse profile from the GAMS-2000 electromagnetic calorimeter data [18]. The above integral equation (8) can be reduced to an Abelian equation by replacing variables [19]. In [20], the following solution to equation (8) was obtained

$$\Phi(r) = -\frac{1}{\pi} \frac{d}{dr^2} \int_{r^2}^{\infty} \frac{f(z) dz^2}{\sqrt{z^2 - r^2}}. \quad (9)$$

For our study, we used the sum of three exponential functions to parameterize  $f(z)$  as

$$f(z) = \frac{E_0}{2B} \sum_{i=1}^3 a_i e^{-\frac{|z|}{\lambda_i}}, \quad (10)$$

where  $z$  is the transverse coordinate,  $E_0$ ,  $a_i$ ,  $\lambda_i$  are free parameters,  $B = \sum_{i=1}^3 a_i \lambda_i$ ,  $\sum_{i=1}^3 a_i = 1$  and  $\int_{-\infty}^{+\infty} f(z) dz = E_0$ . In this case, the radial density function, obtained by integration and differentiation of equation (9), is

$$\Phi(r) = \frac{E_0}{2\pi B} \sum_{i=1}^3 \frac{a_i}{\lambda_i} K_0\left(\frac{r}{\lambda_i}\right), \quad (11)$$

where  $K_0$  is the modified Bessel function. This function goes to  $\infty$  as  $r \rightarrow 0$  and goes to zero as  $r \rightarrow \infty$ .

We define a column of five cells in a depth segment as a tower. Using the parametrization shown in equation (10), we can show that the energy deposition in a tower [21],  $E(z) = \int_{z-h/2}^{z+h/2} f(z) dz$ , can be written as

$$E(z) = E_0 - \frac{E_0}{B} \sum_{i=1}^3 a_i \lambda_i \cosh\left(\frac{|z|}{\lambda_i}\right) e^{-\frac{h}{2\lambda_i}}, \quad \text{for } |z| \leq \frac{h}{2}, \quad (12)$$

$$E(z) = \frac{E_0}{B} \sum_{i=1}^3 a_i \lambda_i \sinh\left(\frac{h}{2\lambda_i}\right) e^{-\frac{|z|}{\lambda_i}}, \quad \text{for } |z| > \frac{h}{2}, \quad (13)$$

where  $h$  is the size of the front face of the tower along the  $z$  axis. Note that as  $h \rightarrow 0$ , we get  $E(z)/h \rightarrow f(z)$ . As  $h \rightarrow \infty$ , we find that  $E(0) \rightarrow E_0$ .

The full width at half maximum (FWHM) of an energy deposition profile for small values of  $(FWHM - h)/h$  can be approximated by

$$FWHM = h + \frac{2E(h/2) - E(0)}{\frac{E_0}{B} \sum_{i=1}^3 a_i \sinh\left(\frac{h}{2\lambda_i}\right) e^{-\frac{h}{2\lambda_i}}}. \quad (14)$$

We will show below that this approximation agrees well with our data.

A cumulative function may be derived from the density function as

$$F(z) = \int_{-\infty}^z f(z) dz. \quad (15)$$

For our parametrization in equation (10), the cumulative function becomes

$$F(z) = \frac{E_0}{2B} \sum_{i=1}^3 a_i \lambda_i e^{\frac{z}{\lambda_i}}, \quad \text{for } z \leq 0, \quad (16)$$

$$F(z) = E_0 - \frac{E_0}{2B} \sum_{i=1}^3 a_i \lambda_i e^{-\frac{z}{\lambda_i}}, \quad \text{for } z > 0, \quad (17)$$

where  $z$  is the position of the edge of a tower along the  $z$  axis. Note that the cumulative function does not depend on the cell size  $h$ . We can construct the cumulative function and deconvolute the density  $f(z)$  from it for any size calorimeter cell. Note also that cumulative function is well behaved at the key points:  $F(-\infty) = 0$ ,  $F(0) = E_0/2$ , and  $F(\infty) = E_0$ .

The radial containment of a shower as a function of  $r$  is given by

$$I(r) = \int_0^r \int_0^{2\pi} \Phi(r) r dr d\phi = E_0 - \frac{E_0 r}{B} \sum_{i=1}^3 a_i K_1\left(\frac{r}{\lambda_i}\right), \quad (18)$$

where  $K_1$  is the modified Bessel function. As  $r \rightarrow \infty$ , the function  $rK_1(r)$  tends to zero and we get  $I(\infty) = E_0$ , as expected.

We use two methods to extract the radial density function  $\Phi(r)$ . One method is to unfold  $\Phi(r)$  from (2). Another method is to use the expression (9) after we have obtained the marginal density function  $f(z)$ . There are three ways to extract  $f(z)$ : by fitting the energy deposition  $E(z)$  [21], by fitting the cumulative function  $F(z)$  and by directly extracting  $f(z)$  by numerical differentiation of the cumulative function. The effectiveness of these various methods depend on the scope and quality of the experimental data.

## 4 Transverse Behaviour of Hadronic Showers

Figure 3 shows the energy depositions in towers for depth segments 1 – 4 as a function of the  $z$  coordinate of the center of the tower. Figure 4 shows the same for the entire calorimeter (the sum of the histograms presented in Fig. 3).

These Figures are profile histograms [13] and give the energy deposited in any tower for all analysed events in bins of the  $z$  coordinate. Here the coordinate system is linked to the incident particle direction where  $z = 0$  is the coordinate of the beam impact points at the calorimeter front face. Figure 5 schematically shows a top view of the experimental setup and indicates the  $z$  coordinate of each tower. The  $z_1, z_2, z_3$  and  $z_4$  are the distances between

the centre of towers (for the four depth segments) and the direction of beam particle. The values of the  $z$ -coordinate of the tower centers are negative to the left of the beam, positive to the right of the beam and range from  $-750$  mm to  $+600$  mm. To avoid edge effects, we present tower energy depositions in the range from  $-650$  mm to  $+500$  mm. Note that the total tower height (about 1.0 m at the front face, and about 1.8 m at the back) is sufficient for shower measurements without significant leakage in the vertical direction.

As mentioned earlier, events with significant lateral leakage (identified by a clear minimum-ionising signal in the lateral muon wall) were discarded. The resulting left-right asymmetries in the distributions of Figures 3 and 4 are very small.

As will be shown later (Section 6), the 99% containment radius is less than 500 mm.

The fine-grained  $z$ -scan provided many different beam impact locations within the calorimeter. Due to this, we obtained a detailed picture of the transverse shower behaviour in the calorimeter. The tower energy depositions shown in Figures 3 and 4 span a range of about three orders of magnitude. The plateau for  $|z| < 100$  mm ( $h/2$ ) and the fall-off at large  $|z|$  are apparent. Similar behaviour of the transverse profiles was observed in other calorimeters as well [16], [21].

We used the distributions in Figs. 3 and 4 to extract the underlying marginal densities function for four depth segments of the calorimeter and for the entire calorimeter. The solid curves in these figures are the results of the fit with equations (12) and (13). The fits typically differ from the experimental distribution by less than 5%.

In comparison with [21] and [22], where the transverse profiles exist only for distances less than 250 mm, our more extended profiles (up to 650 mm) require that the third exponential term be introduced. The parameters  $a_i$  and  $\lambda_i$ , obtained by fitting, are listed in Table 1. The values of the parameter  $E_0$ , the average energy shower deposition in a given depth segment, are listed in Table 4.

We have compared our values of  $\lambda_1$  and  $\lambda_2$  with the ones from the conventional iron-scintillator calorimeter described in [22]. At 100 GeV, our results for the entire calorimeter are  $23 \pm 1$  mm and  $58 \pm 4$  mm for  $\lambda_1$  and  $\lambda_2$  respectively. They agree well with the ones from [22], which are  $18 \pm 3$  mm and  $57 \pm 4$  mm.

We determined the FWHM of energy deposition profiles (Figs. 3 and 4) using formula (14). The characteristic FWHM are found to be approximately equal to transverse tower size. The relative difference of FWHM from transverse tower size,  $(FWHM - h)/h$ , amount to 2% for depth segment 1, depth segment 2 and for the entire calorimeter, 7% for depth segment 3 and 15% for depth segment 4.

Figure 6 shows the calculated marginal density function  $f(z)$  and the energy deposition function,  $E(z)/h$ , at various transverse sizes of tower  $h = 50, 200, 300$  and  $800$  mm using the obtained parameters for the entire calorimeter. As a result of the volume integration, the sharp  $f(z)$  is transformed to the wide function  $E(z)/h$ , which clearly shows its relationship to the transverse width of a tower. The values of FWHM are 40 mm for  $f(z)$  and 204 mm for  $E(z)/h$  at  $h = 200$  mm. Note that the transverse dimensions of a tower vary from 300 mm to 800 mm for the different depth segments in final ATLAS Tile calorimeter design. The difference between  $f(0)$  and  $E(0)/h$  becomes less than 5% only at  $h$  less than 6 mm.

The parameters  $a_i$  and  $\lambda_i$  as a function of  $x$  (in units of  $\lambda_\pi^{Fe}$ ) are displayed in Figs. 7 and 8. Here  $\lambda_\pi^{Fe} = 207$  mm is the nuclear interaction length for pions in iron [20]. In these calculations, the effect of the  $10^\circ$  incidence beam angle has been corrected. As can be seen from Figs. 7 and 8, the value of  $a_1$  decreases and the values of the remaining parameters,  $a_2, a_3$  and  $\lambda_i$ , increase as the shower develops. This is a reflection of the fact that as the hadronic shower propagates into the calorimeter it becomes broader. Note also that the  $a_i$  and  $\lambda_i$  parameters demonstrate linear behaviour as a function of  $x$ . The lines shown are fits

to the linear equations

$$a_i(x) = \alpha_i + \beta_i x \quad (19)$$

and

$$\lambda_i(x) = \gamma_i + \delta_i x. \quad (20)$$

The values of the parameters  $\alpha_i$ ,  $\beta_i$ ,  $\gamma_i$  and  $\delta_i$  are presented in Table 2. It is interesting to note that the linear behaviour of the slope exponential was also observed for the low-density fine-grained flash chamber calorimeter [4]. However, some non-linear behaviour of the slope of the halo component was demonstrated for the uranium-scintillator *ZEUS* calorimeter at interaction lengths more than  $5 \lambda_I$  [23].

Similar results were obtained for the cumulative function distributions. The cumulative function  $F(z)$  is given by

$$F(z) = \sum_{k=1}^4 F^k(z), \quad (21)$$

where  $F^k(z)$  is the cumulative function for depth segment  $k$ . For each event,  $F^k(z)$  is

$$F^k(z) = \sum_{i=1}^{i_{max}} \sum_{j=1}^5 E_{ijk}, \quad (22)$$

where  $i_{max} = 1, \dots, 5$  is the last tower number in the sum.

Figures 9 and 10 present the cumulative functions for four depth segments and for the entire calorimeter. The curves are fits of equations (16) and (17) to the data. Systematic and statistical errors are again added in quadrature. The results of the cumulative function fits are less reliable and in what follows we use the results from energy depositions in a tower.

However, the marginal density functions determined by the two methods (by using the energy deposition spectrum and the cumulative function) are in reasonable agreement.

## 5 Radial Hadronic Shower Energy Density

Using formula (11) and the values of the parameters  $a_i$ ,  $\lambda_i$ , given in Table 1, we have determined the underlying radial hadronic shower energy density functions,  $\Phi(r)$ . The results are shown in Figure 11 for depth segments 1 – 4 and in Figure 12 for the entire calorimeter. The contributions of the three terms of  $\Phi(r)$  are also shown.

The functions  $\Phi(r)$  for separate depth segments of a calorimeter are given in this paper for the first time. The function  $\Phi(r)$  for the entire calorimeter was previously given for a Lead-scintillating fiber calorimeter [16]; it is given here for the first time for an Iron-scintillator calorimeter. The analytical functions giving the radial energy density for different depth segments allow to easily obtain the shower energy deposition in any calorimeter cell, shower containment fractions and the cylinder radii for any given shower containment fraction.

The function  $\Phi(r)$  for the entire calorimeter has been compared with the one for the lead-scintillating fiber calorimeter of ref. [16], that has about the same effective nuclear interaction length for pions (namely 251 mm for the tile and 244 mm for the fiber calorimeter [20]). The two radial density functions are rather similar as seen in Fig. 13. The lead-scintillating fiber calorimeter density function  $\Phi(r)$ , which was obtained from a 80 GeV  $\pi^-$  grid scan at an angle of  $2^\circ$  with respect to the fiber direction, was parametrized using formula (6) with  $b_1 = 0.169$  pC/mm,  $b_2 = 0.677$  pC/mm,  $\mu_1 = 140$  mm and  $\mu_2 = 42.4$  mm. For the sake of comparing the radial density functions of the two calorimeters, the distribution from [16] was normalised to the  $\Phi(r)$  of the Tile calorimeter. Precise agreement between these functions should not be expected because of the effect of the different absorber materials used in the



two detectors (e. g. the radiation/interaction length ratio for the Tile calorimeter is three times larger than for lead-scintillating fiber calorimeter [20]), the values of  $e/h$  are different, as is hadronic activity of showers because fewer neutrons are produced in iron than in lead [24], [25]).

## 6 Radial Containment

An other issue on which new results are presented here is the longitudinal development of shower transverse dimensions. The parametrization of the radial density function,  $\Phi(r)$ , was integrated to yield the shower containment as a function of the radius,  $I(r)$ . Figure 14 shows the transverse containment of the pion shower,  $I(r)$ , as a function of  $r$  for four depth segments and for the entire calorimeter.

In Table 3 and Fig. 15 the radii of cylinders for the given shower containment (90%, 95% and 99%) extracted from Fig. 14 as a function of depth are shown. The centers of depth segments,  $x$ , are given in units of  $\lambda_\pi^{Fe}$ . Solid lines are the linear fits to the data:  $r(90\%) = (85 \pm 6) + (37 \pm 3)x$ ,  $r(95\%) = (134 \pm 9) + (45 \pm 3)x$ ,  $r(99\%) = (349 \pm 7) + (22 \pm 2)x$  (mm). As can be seen, these containment radii increase linearly with depth. Such a linear increase of 95% lateral shower containment with depth is also observed in an other iron-scintillator calorimeter at 50 and 140 GeV [26]. It is interesting to note that the shower radius for 95% radial containment for the entire calorimeter is equal to  $\lambda_\pi^{eff} = 251$  mm [20] which justifies the frequently encountered statement that  $r(95\%) \approx \lambda_I$  [24], where  $\lambda_I$  is  $\lambda_\pi^{eff}$  in our case. For the entire Tile calorimeter the 99% containment radius is equal to  $1.7 \pm 0.1 \lambda_\pi^{eff}$ .

Based on our study, we believe that it is a poor approximation to regard the values obtained from the marginal density function or the energy depositions in strips as the measure of the transverse shower containment, as was done in [4]. In that paper the value of  $1.1 \lambda_\pi^{eff}$  was obtained for 99% containment at 100 GeV, and the conclusion was drawn that their “result is consistent with the *rule of thumb* that a shower is contained within a cylinder of radius equal to the interaction length of a calorimeter material”. However Tile calorimeter measurements show that the cylinder radius for 99% shower containment is about two interaction lengths. If we extract the lateral shower containment dimension using instead the integrated function  $F(z)$ , given in Fig. 10, we obtain the value of 300 mm or  $1.2 \lambda_\pi^{eff}$ , which agrees with [4].

## 7 Longitudinal Profile

We have examined the differential deposition of energy  $\Delta E/\Delta x$  as a function of  $x$ , the distance along the shower axis. Table 4 lists the centers in  $x$  of the depth segments,  $x$ , and the lengths along  $x$  of the depth segments,  $\Delta x$ , in units of  $\lambda_\pi^{Fe}$ , the average shower energy depositions in various depth segments,  $E_0$ , and the energy depositions per interaction length  $\lambda_\pi^{Fe}$ ,  $\Delta E/\Delta x$ . Note that the values of  $E_0$  have been obtained taking into account the longitudinal energy leakage which amounts to 1.8 GeV for 100 GeV [14].

Our values of  $\Delta E/\Delta x$  together with the data of [27] and Monte Carlo predictions (GEANT-FLUKA + MICAP) [28] are shown in Fig. 16. The longitudinal energy deposition for our calorimeter using longitudinal orientation of the scintillating tiles is in good agreement with that of a conventional iron-scintillator calorimeter.

The longitudinal profile,  $\Delta E/\Delta x$ , may be approximated using two parametrizations. The

first form is

$$\frac{dE(x)}{dx} = \frac{E_f \beta^{\alpha+1}}{\Gamma(\alpha+1)} x^\alpha e^{-\beta x} \quad (23)$$

where  $E_f = E_{beam}$ , and  $\alpha$  and  $\beta$  are free parameters. Our data at 100 GeV and those of Ref. [27] at 100 GeV were jointly fit to this expression; the fit is shown in Fig. 16.

The second form is the analytical representation of the longitudinal shower profile from the front of the calorimeter

$$\begin{aligned} \frac{dE(x)}{dx} = N \left\{ \frac{w X_0}{a} \left( \frac{x}{X_0} \right)^a e^{-b \frac{x}{X_0}} {}_1F_1 \left( 1, a+1, \left( b - \frac{X_0}{\lambda_I} \right) \frac{x}{X_0} \right) \right. \\ \left. + \frac{(1-w) \lambda_I}{a} \left( \frac{x}{\lambda_I} \right)^a e^{-d \frac{x}{\lambda_I}} {}_1F_1 \left( 1, a+1, (d-1) \frac{x}{\lambda_I} \right) \right\}, \quad (24) \end{aligned}$$

where  ${}_1F_1$  is the confluent hypergeometric function [29]. Here the depth variable,  $x$ , is the depth in equivalent  $Fe$ ,  $X_0$  is the radiation length in  $Fe$  and in this case  $\lambda_I$  is  $\lambda_\pi^{Fe}$ . The normalisation factor,  $N$ , is given by

$$N = E_{beam} / \int_0^\infty \frac{dE(x)}{dx} dx = \frac{E_{beam}}{\lambda_I \Gamma(a) (w X_0 b^{-a} + (1-w) \lambda_I d^{-a})}. \quad (25)$$

This form was suggested in [30] and derived by integration over the shower vertex positions of the longitudinal shower development from the shower origin

$$\frac{dE(x)}{dx} = \int_0^x \frac{dE_s(x-x_v)}{dx} e^{-\frac{x_v}{\lambda_I}} dx_v, \quad (26)$$

where  $x_v$  is the coordinate of the shower vertex. (This is necessary because with the Tile calorimeter longitudinal segmentation the shower vertex is not measured). For the parametrization of longitudinal shower development, the well known parametrization suggested by Bock et al. [5] has been used

$$\frac{dE_s(x)}{dx} = N \left\{ w \left( \frac{x}{X_0} \right)^{a-1} e^{-b \frac{x}{X_0}} + (1-w) \left( \frac{x}{\lambda_I} \right)^{a-1} e^{-d \frac{x}{\lambda_I}} \right\}, \quad (27)$$

where  $a$ ,  $b$ ,  $d$ ,  $w$  are parameters.

We compare the form (24) to the experimental points at 100 GeV using the parameters calculated in Refs. [5] and [27]. Note that now we are not performing a fit but checking how well the general form (24) together with two sets of parameters for iron-scintillator calorimeters describe our data. As shown in Fig. 16, both sets of parameters work rather well in describing the 100 GeV data.

Turning next to the longitudinal shower development at different energies, in Fig. 17 our values of  $\Delta E/\Delta x$  for 20 – 300 GeV together with the data from [27] are shown. The solid and dashed lines are calculations with function (24) using parameters from [27] and [5], respectively. Again, we observe reasonable agreement between our data and the corresponding data for conventional iron-scintillator calorimeter on one hand, and between data and the parametrizations described above. Note that the fit in [27] has been performed in the energy range from 10 to 140 GeV; hence the curves for 200 and 300 GeV should be considered as extrapolations. It is not too surprising that at these energies the agreement is significantly worse, particularly at 300 GeV. In contrast, the parameters of [5] were derived from data spanning the range 15 – 400 GeV, and are in much closer agreement with our data.

## 8 The parametrization of Hadronic Showers

The three-dimensional parametrization for spatial hadronic shower development is

$$\Psi(x, r) = \frac{dE(x)}{dx} \cdot \frac{\sum_{i=1}^3 \frac{a_i(x)}{\lambda_i(x)} K_0\left(\frac{r}{\lambda_i(x)}\right)}{2\pi \sum_{i=1}^3 a_i(x)\lambda_i(x)}, \quad (28)$$

where  $dE(x)/dx$ , defined by equation (24), is the longitudinal energy deposition, the functions  $a_i(x)$  and  $\lambda_i(x)$  are given by equations (19) and (20), and  $K_0$  is the modified Bessel function.

This explicit three dimensional parametrization can be used as a convenient tool for many calorimetry problems requiring the integration of a shower energy deposition in a volume and the reconstruction of the shower coordinates.

## 9 Electromagnetic Fraction of Hadronic Showers

One of the important issues in the understanding of hadronic showers is the electromagnetic component of the shower, i. e. the fraction of energy going into  $\pi^0$  production and its dependence on radial and longitudinal coordinates,  $f_{\pi^0}(r, x)$ . Following [16], we assume that the electromagnetic part of a hadronic shower is the prominent central core, which in our case is the first term in the expression (11) for the radial energy density function,  $\Phi(r)$ . Integrating  $f_{\pi^0}$  over  $r$  we get

$$f_{\pi^0} = \frac{a_1 \lambda_1}{\sum_{i=1}^3 a_i \lambda_i}. \quad (29)$$

For the entire Tile calorimeter this value is  $(53 \pm 3)\%$  at 100 GeV.

The observed  $\pi^0$  fraction,  $f_{\pi^0}$ , is related to the intrinsic actual fraction,  $f'_{\pi^0}$ , by the equation

$$f_{\pi^0}(E) = \frac{e E'_{em}}{e E'_{em} + h E'_h} = \frac{e/h \cdot f'_{\pi^0}(E)}{(e/h - 1) \cdot f'_{\pi^0}(E) + 1}, \quad (30)$$

where  $E'_{em}$  and  $E'_h$  are the intrinsic electromagnetic and hadronic parts of shower energy,  $e$  and  $h$  are the coefficients of conversion of intrinsic electromagnetic and hadronic energies into observable signals,  $f'_{\pi^0} = E'_{em}/(E'_{em} + E'_h)$ .

There are two analytic forms for the intrinsic  $\pi^0$  fraction suggested by Groom [31]

$$f'_{\pi^0}(E) = 1 - \left(\frac{E}{E'_0}\right)^{m-1} \quad (31)$$

and Wigmans [32]

$$f'_{\pi^0}(E) = k \cdot \ln\left(\frac{E}{E'_0}\right), \quad (32)$$

where  $E'_0 = 1$  GeV,  $m = 0.85$  and  $k = 0.11$ . We calculated  $f_{\pi^0}$  using the value  $e/h = 1.34 \pm 0.03$  for our calorimeter [2], [33] and obtained the curves shown in Fig. 18.

Our result at 100 GeV is compared in Fig. 18 to the modified Groom and Wigmans parametrizations and to results from the Monte Carlo codes CALOR [25], GEANT-GEISHA [28] and GEANT-CALOR [34] (the latter code is an implementation of CALOR89 differing from GEANT-FLUKA only for hadronic interactions below 10 GeV). Note that the Monte Carlo calculations were performed for the intrinsic  $\pi^0$  fraction,  $f'_{\pi^0}(E)$ , and therefore the

results were modified by us according to (30). As can be seen from Fig. 18, our calculated value of  $f_{\pi^0}$  is about one standard deviation lower than two of the Monte Carlo results and the Groom and Wigmans parametrizations.

Figure 19 shows the fractions  $f_{\pi^0}(r)$  as a function of  $r$ . As can be seen, the fractions  $f_{\pi^0}(r)$  for the entire calorimeter and for depth segments 1 – 3 amount to about 90% as  $r \rightarrow 0$  and decrease to about 1% as  $r \rightarrow \lambda_{\pi}^{eff}$ . However for depth segment 4 the value of  $f_{\pi^0}(r)$  amounts to only 50% as  $r \rightarrow 0$  and decreases slowly to about 10% as  $r \rightarrow \lambda_{\pi}^{eff}$ .

Figure 20 shows the values of  $f_{\pi^0}(x)$  as a function of  $x$ , as well as the linear fit which gives  $f_{\pi^0}(x) = (75 \pm 2) - (8.4 \pm 0.4)x$  (%).

Using the values of  $f_{\pi^0}(x)$  and energy depositions for various depth segments, we obtained the contributions from the electromagnetic and hadronic parts of hadronic showers in Fig. 16. The curves represent a fit to the electromagnetic and hadronic components of the shower using equation (23).  $E_f$  is set equal to  $f_{\pi^0}E_{beam}$  for the electromagnetic fraction and  $(1 - f_{\pi^0})E_{beam}$  for the hadronic fraction. The electromagnetic component of a hadronic shower rise and decrease more rapidly than the hadronic one ( $\alpha_{em} = 1.4 \pm 0.1$ ,  $\alpha_h = 1.1 \pm 0.1$ ,  $\beta_{em} = 1.12 \pm 0.04$ ,  $\beta_h = 0.65 \pm 0.05$ ). The shower maximum position ( $x_{max} = (\alpha/\beta) \lambda_{\pi}^{eff}$ ) occurs at a shorter distance from the calorimeter front face ( $x_{max}^{em} = 1.23 \lambda_{\pi}^{eff}$ ,  $x_{max}^h = 1.85 \lambda_{\pi}^{eff}$ ). At depth segments greater than 4  $\lambda_{\pi}^{eff}$ , the hadronic fraction of the shower begins to dominate. This is natural since the energy of the secondary hadrons is too low to permit significant pion production.

## 10 Summary and Conclusions

We have investigated the lateral development of hadronic showers using 100 GeV pion beam data at an incidence angle of  $\Theta = 10^\circ$  for impact points  $z$  in the range from  $-360$  to  $200$  mm and the longitudinal development of hadronic showers using  $20 - 300$  GeV pion beams at an incidence angle of  $\Theta = 20^\circ$ .

Some useful formulae for the investigation of lateral profiles have been derived using a three-exponential form of the marginal density function  $f(z)$ .

We have obtained for four depth segments and for the entire calorimeter: energy depositions in towers,  $E(z)$ ; cumulative functions,  $F(z)$ ; underlying radial energy densities,  $\Phi(r)$ ; the contained fraction of a shower as a function of radius,  $I(r)$ ; the radii of cylinders for a given shower containment fraction; the fractions of the electromagnetic and hadronic parts of a shower; differential longitudinal energy deposition  $\Delta E/\Delta x$ ; and a three-dimensional hadronic shower parametrization.

We have compared our data with those from a conventional iron-scintillator calorimeter, those from a lead-scintillator fiber calorimeter, and with Monte Carlo calculations. We have found that there is general reasonable agreement in the behaviour of the Tile calorimeter radial density functions and those of the lead-scintillating fiber calorimeter; that the longitudinal profile agrees with that of a conventional iron-scintillator calorimeter and the Monte Carlo predictions; that the value at 100 GeV of the calculated fraction of energy going into  $\pi^0$  production in a hadronic shower,  $f_{\pi^0}$ , agrees with the Groom and Wigmans parametrizations and with some of the Monte Carlo predictions.

The three-dimensional parametrization of hadronic showers that we obtained allows direct use in any application that requires volume integration of shower energy depositions and position reconstruction. The experimental data on the transverse and longitudinal profiles, the radial energy densities and the three-dimensional hadronic shower parametrization are useful for understanding the performance of the Tile calorimeter, but might find broader application in Monte Carlo modeling of hadronic showers, in particular in fast simulations,

and for future calorimeter design.

## 11 Acknowledgements

This paper is the result of the efforts of many people from the ATLAS Collaboration. The authors are greatly indebted to the entire Collaboration for their test beam setup and data taking. We are grateful to the staff of the SPS, and in particular to Konrad Elsener, for the excellent beam conditions and assistance provided during our tests.

## References

- [1] ATLAS Collaboration, ATLAS Technical Proposal for a General-Purpose pp Experiment at the Large Hadron Collider, CERN/LHCC/94-93, CERN, Geneva, Switzerland, 1994.
- [2] ATLAS Collaboration, ATLAS Tile Calorimeter Technical Design Report, ATLAS TDR 3, CERN/LHCC/96-42, CERN, Geneva, Switzerland, 1996.
- [3] R.K. Bock and A. Vasilescu, *The Particle Detector Briefbook*, Springer, 1998.
- [4] W.J. Womersley *et al.*, NIM A267 (1988) 49.
- [5] R.K. Bock *et al.*, NIM 186 (1981) 533.
- [6] G. Grindhammer *et al.*, NIM A289 (1990) 469.
- [7] R. Brun *et al.*, *Proceedings of the Second Int. Conf. on Calorimetry in HEP*, p. 82, Capri, Italy, 1991.
- [8] E. Berger *et al.*, CERN/LHCC 95-44, CERN, Geneva, Switzerland, 1995.
- [9] M. Lokajicek *et al.*, ATLAS Internal Note<sup>1</sup>, TILECAL-No-64, CERN, Geneva, Switzerland, 1995.
- [10] F. Ariztizabal *et al.*, NIM A349 (1994) 384.
- [11] M. Lokajicek *et al.*, ATLAS Internal Note, TILECAL-No-63, CERN, Geneva, Switzerland, 1995.
- [12] I. Efthymiopoulos, A. Solodkov, *The TILECAL Program for Test Beam Data Analysis*, ATLAS Internal Note, TILECAL-No-101, CERN, Geneva, Switzerland, 1996.
- [13] Application Software Group, PAW — *Physics Analysis Workstation*, CERN Program Library, entry Q121, CERN, Geneva, Switzerland, 1995.
- [14] J.A. Budagov, Y.A. Kulchitsky, V.B. Vinogradov *et al.*, JINR, E1-96-180, Dubna, Russia, 1996; ATLAS Internal note, TILECAL-No-76, CERN, Geneva, Switzerland, 1996.
- [15] R.M. Barnett *et al.*, *Review of Particle Physics, Probability*, Phys. Rev. D54 (1996).
- [16] D. Acosta *et al.*, NIM A316 (1992) 184.

---

<sup>1</sup> An Internet version of ATLAS Tile calorimeter Internal notes in postscript format are available at URL [http://atlasinfo.cern.ch/Atlas/SUB\\_DETECTORS/TILE/tileref/tinotes.html](http://atlasinfo.cern.ch/Atlas/SUB_DETECTORS/TILE/tileref/tinotes.html)

- [17] A.A. Lednev *et al.*, NIM A366 (1995) 292.
- [18] G.A. Akopdijanov *et al.*, NIM 140 (1977) 441.
- [19] E.T. Whittaker, G.N. Watson, A Course of Modern Analysis, Cambridge, Univ. Press, 1927.
- [20] J.A. Budagov, Y.A. Kulchitsky, V.B. Vinogradov *et al.*, JINR, E1-97-318, Dubna, Russia, 1997; ATLAS Internal note, TILECAL-No-127, CERN, Geneva, Switzerland, 1997.
- [21] O.P. Gavrishchuk *et al.*, JINR, P1-91-554, Dubna, Russia, 1991.
- [22] F. Binon *et al.*, NIM A206 (1983) 373.
- [23] F. Barreiro *et al.*, NIM A292 (1990) 259.
- [24] C.W. Fabjan and T. Ludlam, Calorimetry in High-Energy Physics, Ann. Rev. Nucl. Part. Sci. 32 (1982).
- [25] T.A. Gabriel *et al.*, NIM A338 (1994) 336.
- [26] M. Holder *et al.*, NIM 151 (1978) 69.
- [27] E. Hughes, Proc. of the I Int. Conf. on Calor. in HEP, p. 525, FNAL, Batavia, 1990.
- [28] A. Juste, ATLAS Internal note, TILECAL-No-69, CERN, Geneva, Switzerland, 1995.
- [29] M. Abramovitz and I.A. Stegun (Eds.), Handbook of Mathematical Functions, National Bureau of Standards, Applied Mathematics, N.Y., Columbia Univ. Press, 1964.
- [30] Y.A. Kulchitsky, V.B. Vinogradov, NIM A413 (1998) 484.
- [31] D. Groom, Proceedings of the Workshop on Calorimetry for the Supercollider, Tuscaloosa, Alabama, USA, 1990.
- [32] R. Wigmans, NIM A265 (1988) 273.
- [33] J.A. Budagov, Y.A. Kulchitsky, V.B. Vinogradov *et al.*, JINR, E1-95-513, Dubna, Russia, 1995; ATLAS Internal note, TILECAL-No-72, CERN, Geneva, Switzerland, 1995.
- [34] M. Bosman, *Establishing Requirements from the Point of View of the ATLAS Hadronic Barrel Calorimeter*, ATLAS Workshop on Shower Models, 15 – 16 September 1997, CERN, Geneva, Switzerland, 1997.

Table 1: The parameters  $a_i$  and  $\lambda_i$  obtained by fitting the transverse shower profiles for four depth segments and the entire calorimeter at 100 GeV.

Depth	$x (\lambda_\pi^{Fe})$	$a_1$	$\lambda_1$ (mm)	$a_2$	$\lambda_2$ (mm)	$a_3$	$\lambda_3$ (mm)
1	0.6	$0.88 \pm 0.07$	$17 \pm 2$	$0.12 \pm 0.07$	$48 \pm 14$	$0.004 \pm 0.002$	$430 \pm 240$
2	2.0	$0.79 \pm 0.06$	$25 \pm 2$	$0.20 \pm 0.06$	$52 \pm 6$	$0.014 \pm 0.006$	$220 \pm 40$
3	3.8	$0.69 \pm 0.03$	$32 \pm 8$	$0.28 \pm 0.03$	$71 \pm 13$	$0.029 \pm 0.005$	$280 \pm 30$
4	6.0	$0.41 \pm 0.05$	$51 \pm 10$	$0.52 \pm 0.06$	$73 \pm 18$	$0.07 \pm 0.03$	$380 \pm 140$
all four		$0.78 \pm 0.08$	$23 \pm 1$	$0.20 \pm 0.08$	$58 \pm 4$	$0.015 \pm 0.004$	$290 \pm 40$

Table 2: The values of the parameters  $\alpha_i$ ,  $\beta_i$ ,  $\gamma_i$  and  $\delta_i$ .

	$\alpha_i$	$\beta_i (1/\lambda_\pi)$		$\gamma_i$ (mm)	$\delta_i$ (mm/ $\lambda_\pi$ )
$a_1$	$0.99 \pm 0.06$	$-0.088 \pm 0.015$	$\lambda_1$	$13 \pm 2$	$6 \pm 1$
$a_2$	$0.04 \pm 0.06$	$0.071 \pm 0.015$	$\lambda_2$	$42 \pm 10$	$6 \pm 4$
$a_3$	$-0.001 \pm 0.002$	$0.008 \pm 0.002$	$\lambda_3$	$170 \pm 80$	$29 \pm 23$

Table 3: The radii of cylinders for the given shower containment at 100 GeV.

$x (\lambda_{\pi}^{Fe})$	$r (\lambda_{\pi}^{eff})$		
	90%	95%	99%
0.6	0.44	0.64	1.43
2.0	0.60	0.88	1.55
3.8	0.92	1.27	1.75
6.0	1.24	1.55	1.87
all four	0.72	1.04	1.67

Table 4: Average energy shower depositions at various depth segments at 100 GeV.

$x (\lambda_{\pi}^{Fe})$	$\Delta x (\lambda_{\pi}^{Fe})$	$E_0$ (GeV)	$\Delta E/\Delta x$ (GeV/ $\lambda_{\pi}^{Fe}$ )
0.6	1.2	25.0±0.3	20.8±0.3
2.0	1.6	42.8±0.2	26.8±0.1
3.8	2.0	22.0±0.1	11.0±0.1
6.0	2.4	8.4±0.5	3.4±0.2



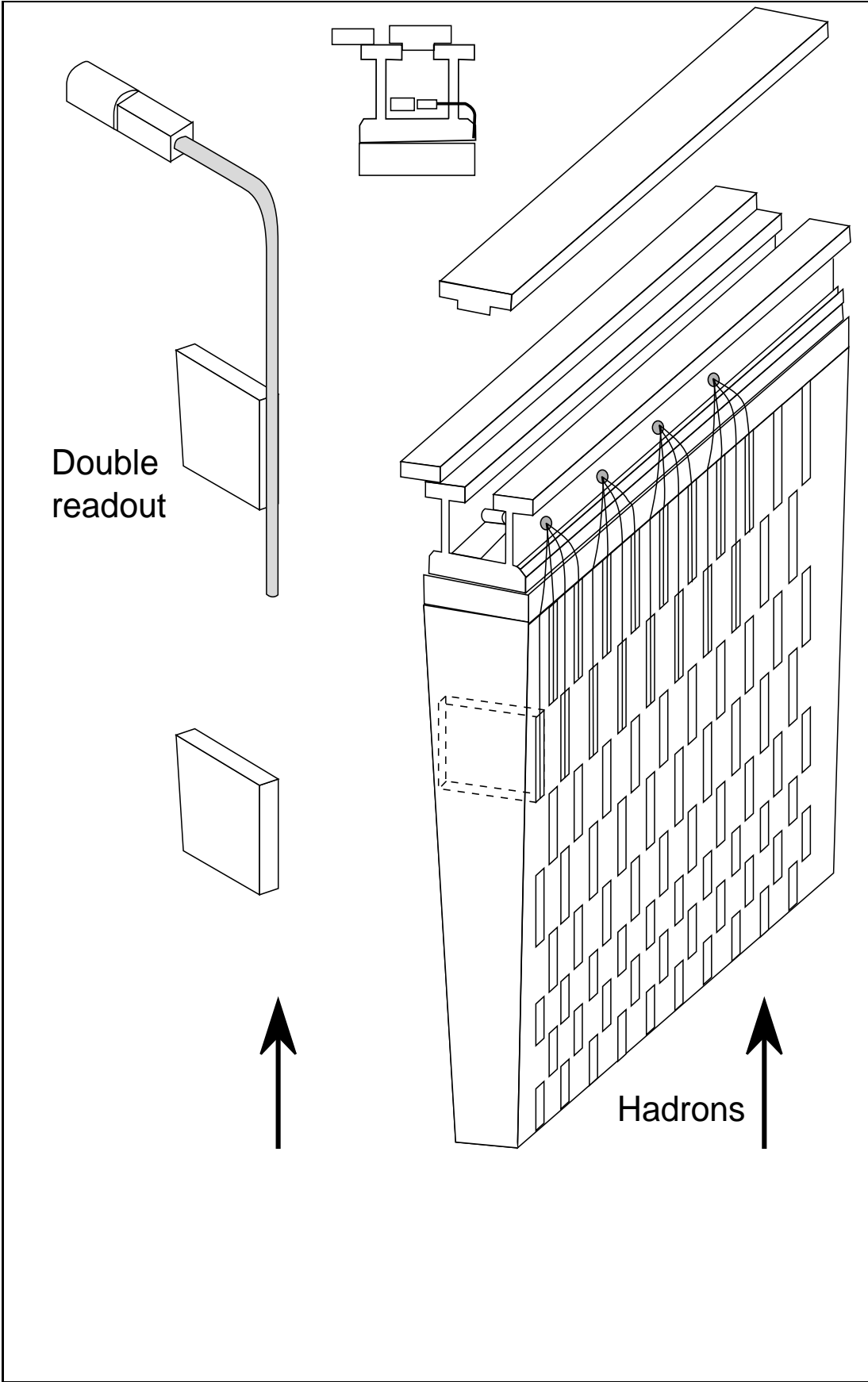


Figure 1: Conceptual design of a Tile calorimeter module.

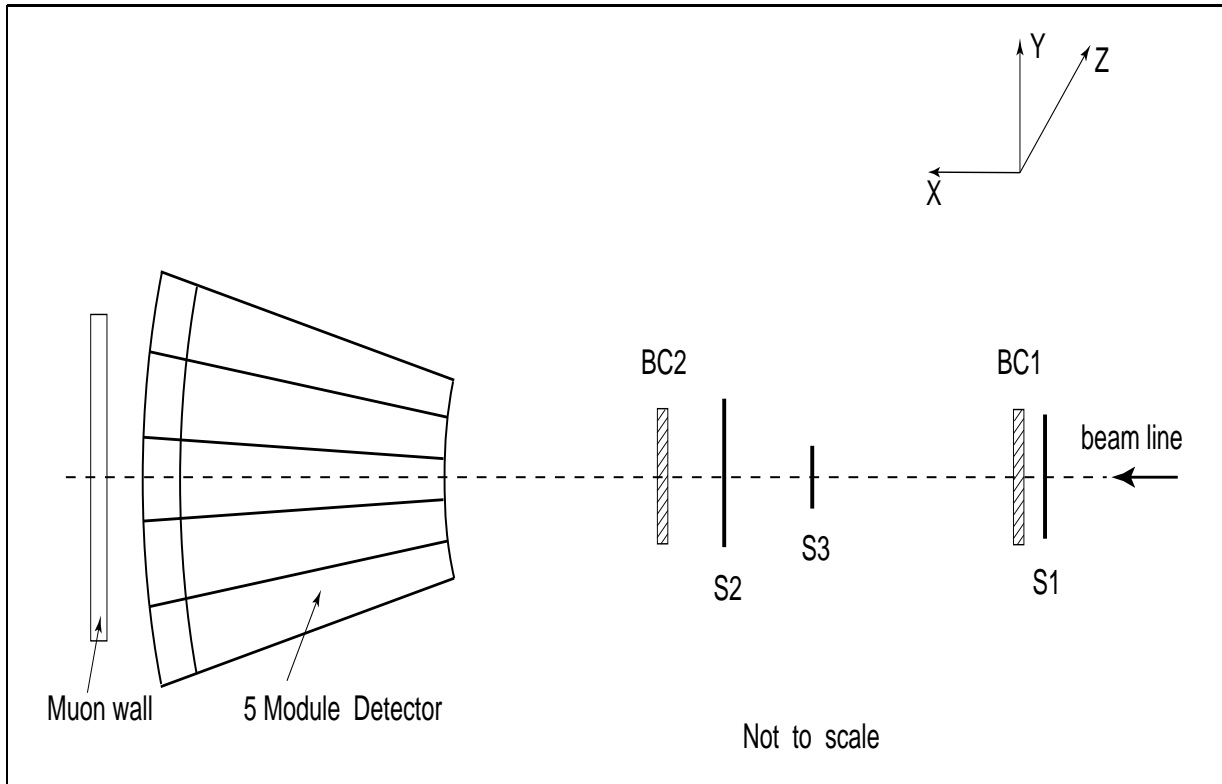


Figure 2: Schematic layout of the experimental setup. S1 – S3 are beam trigger scintillators, and BC1 – BC2 are (Z,Y) proportional chambers.

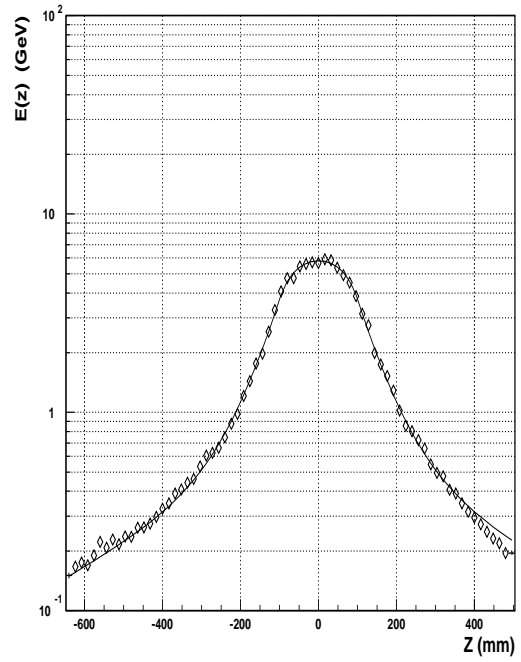
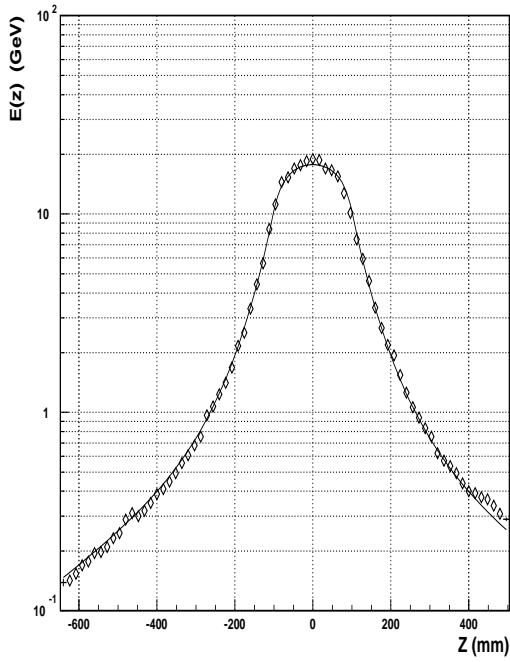
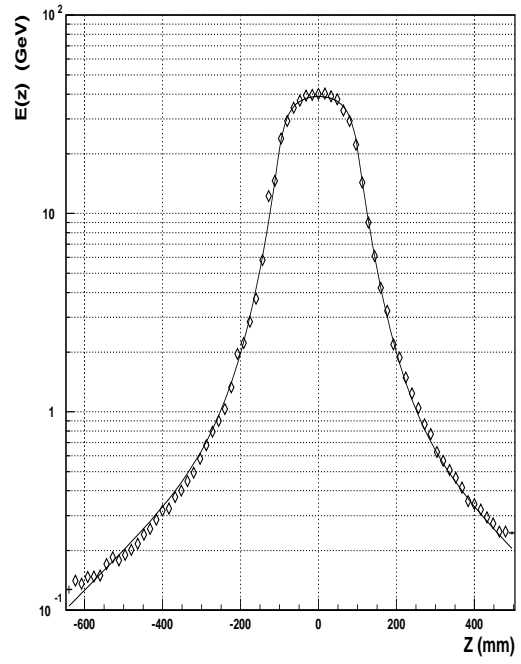
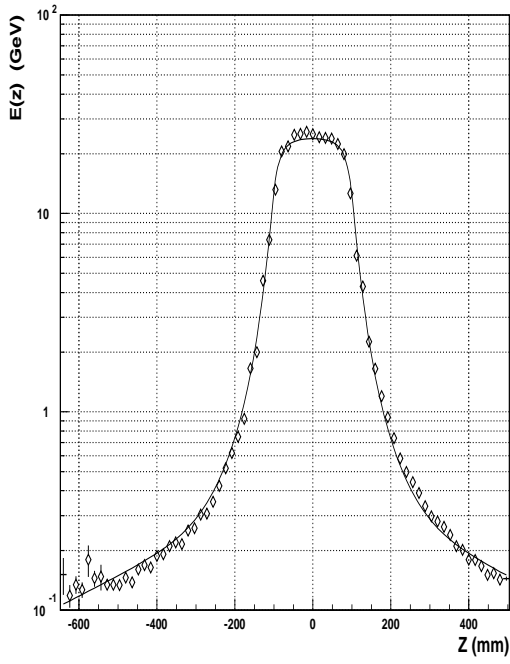


Figure 3: Energy depositions of 100 GeV pions in towers of depth segments 1 – 4 as a function of the  $z$  coordinate: top left is for depth segment 1, top right is for depth segment 2, bottom left is for depth segment 3, bottom right is for depth segment 4. Only statistical errors are shown. Curves are fits of equations (12) and (13) to the data.

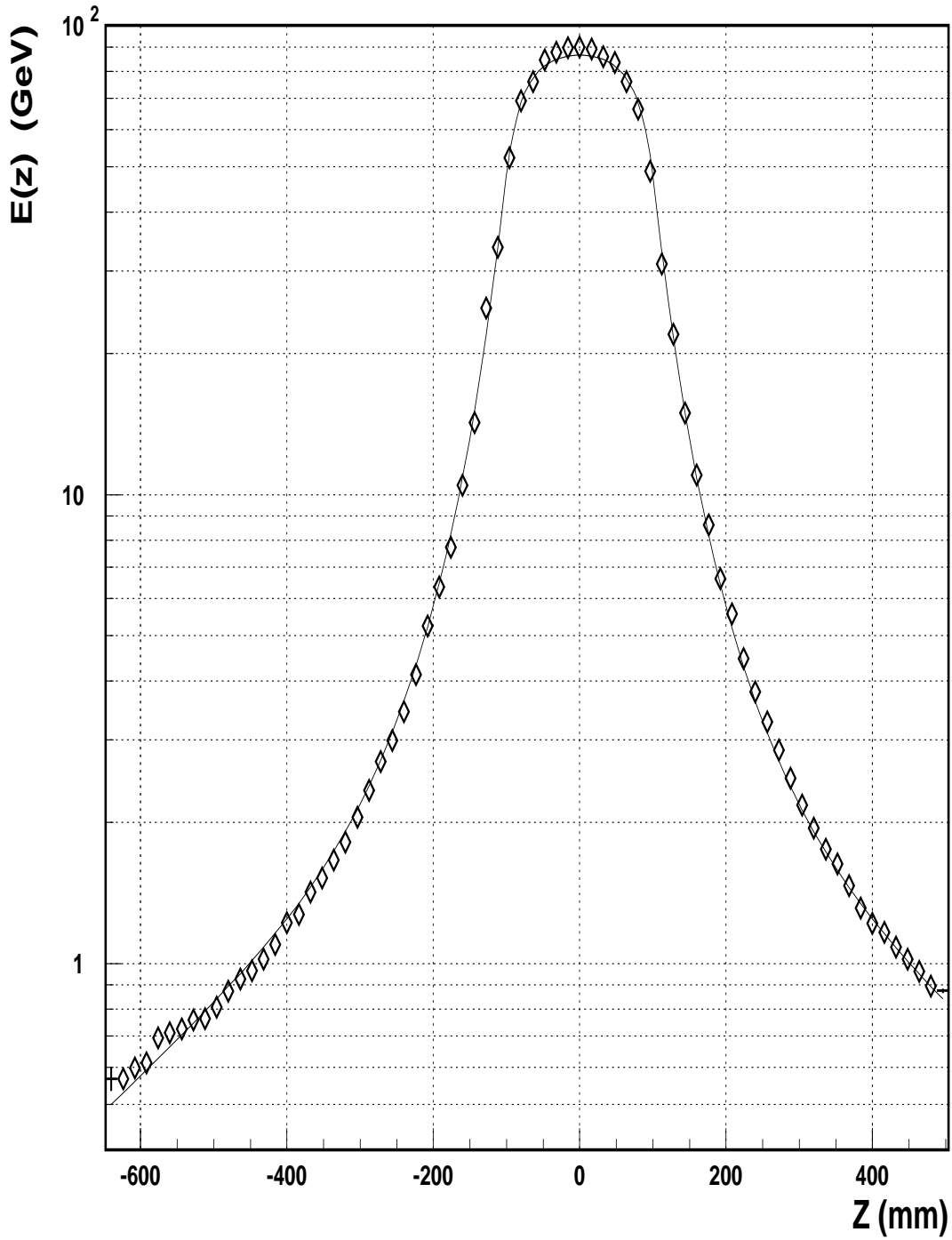


Figure 4: Energy depositions in towers, summed over all calorimeter depth segments, as a function of the  $z$  coordinate. Only statistical errors are shown. The curve is the result of the fit by formulas (12) and (13).

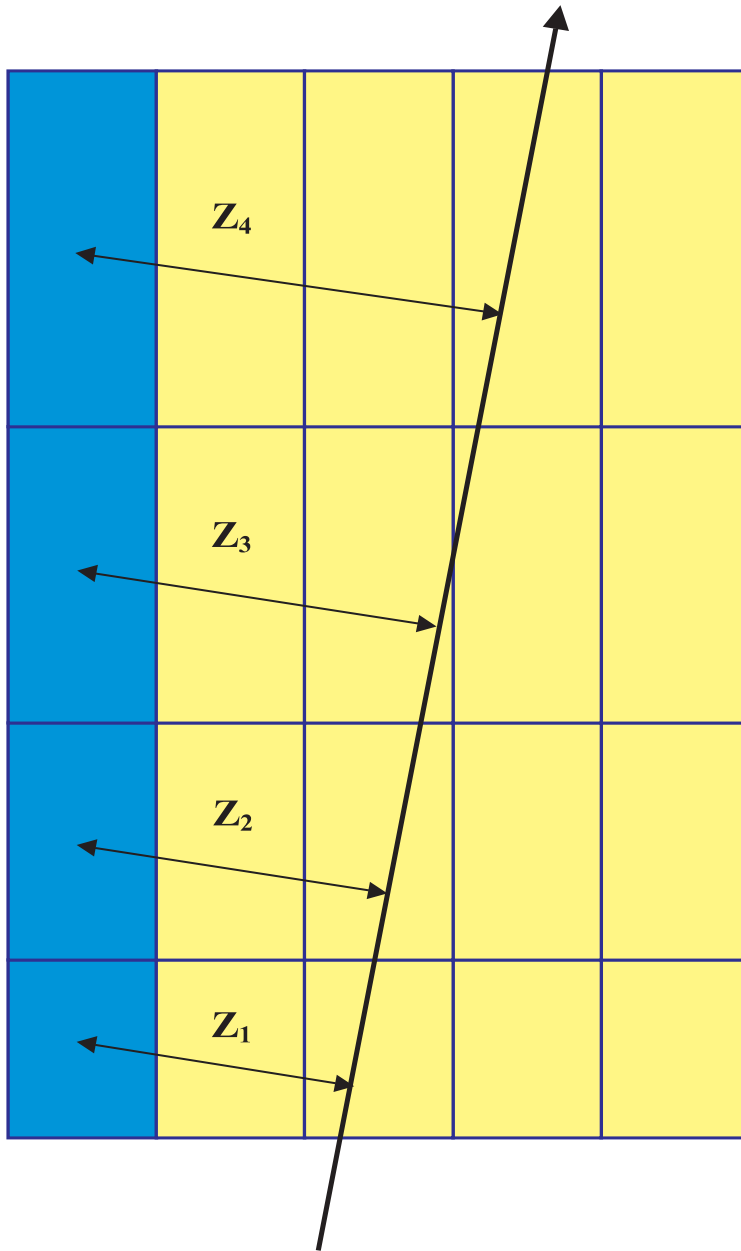


Figure 5: Schematic layout (top view) of Tile calorimeter experimental setup.  $z_1 - z_4$  are the distances between the centre of towers (for the four depth segments) and the direction of the beam particle.

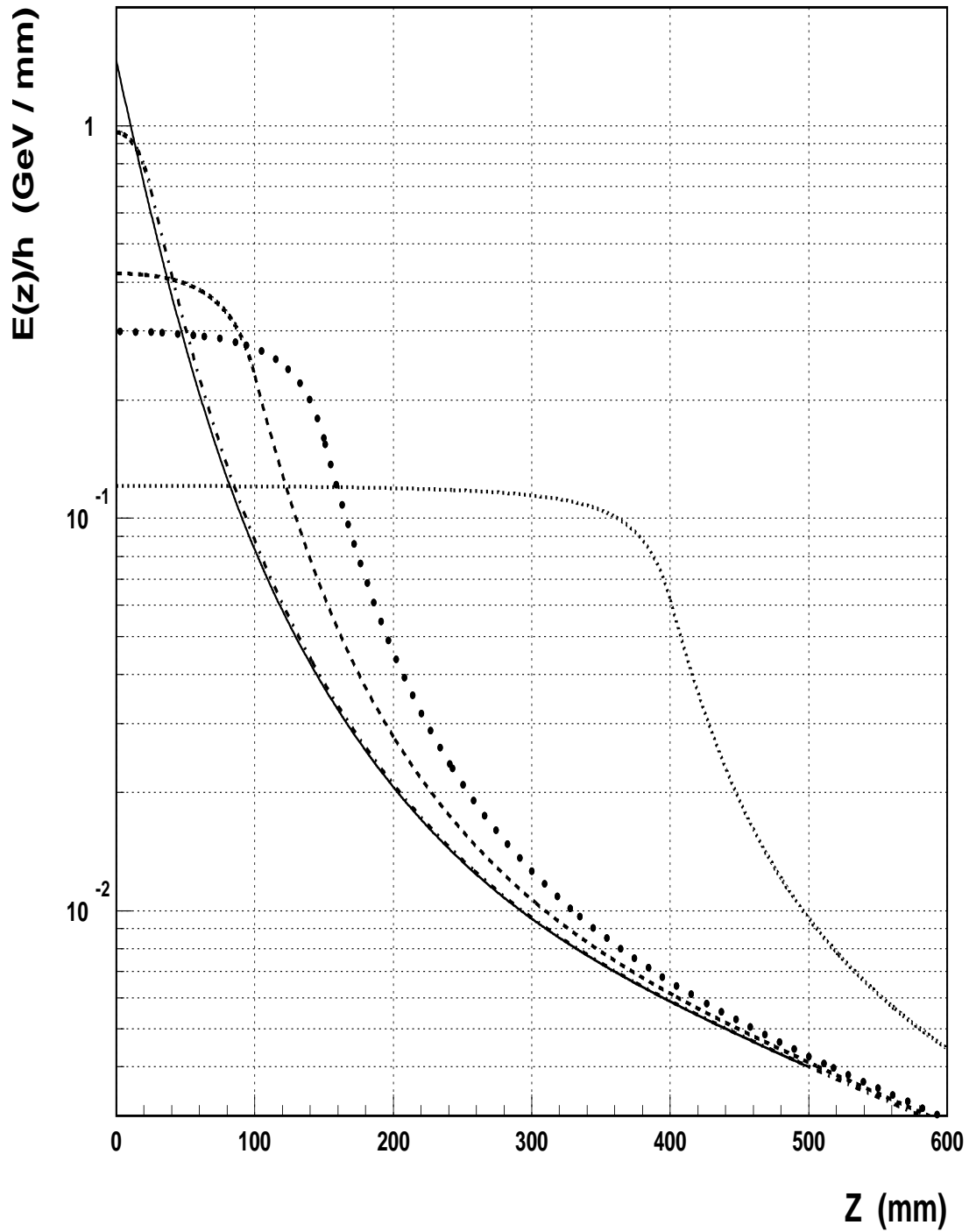


Figure 6: The calculated marginal density function  $f(z)$  (the solid line) and the energy deposition function,  $E(z)/h$ , for various transverse sizes of a tower ( $h$ ): 50 mm (the dash-dotted line), 200 mm (the dashed line), 300 mm (the thick dotted line), 800 mm (the thin dotted line). The parameters for the entire calorimeter (see Table 1) are used in the calculations.

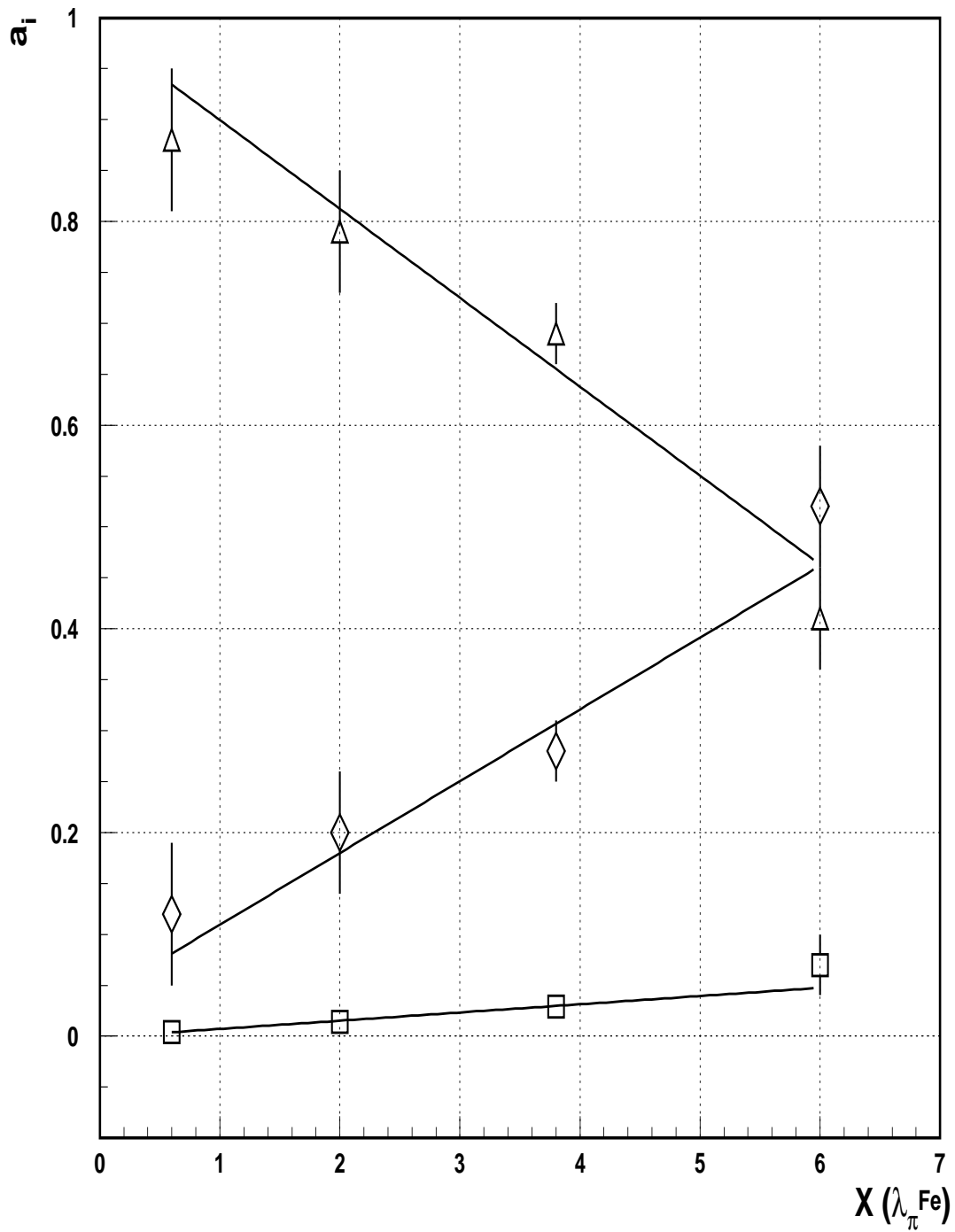


Figure 7:  $X$  dependences of the parameters  $a_i$ : the triangles are the  $a_1$  parameter, the diamonds are the  $a_2$ , the squares are the  $a_3$ .

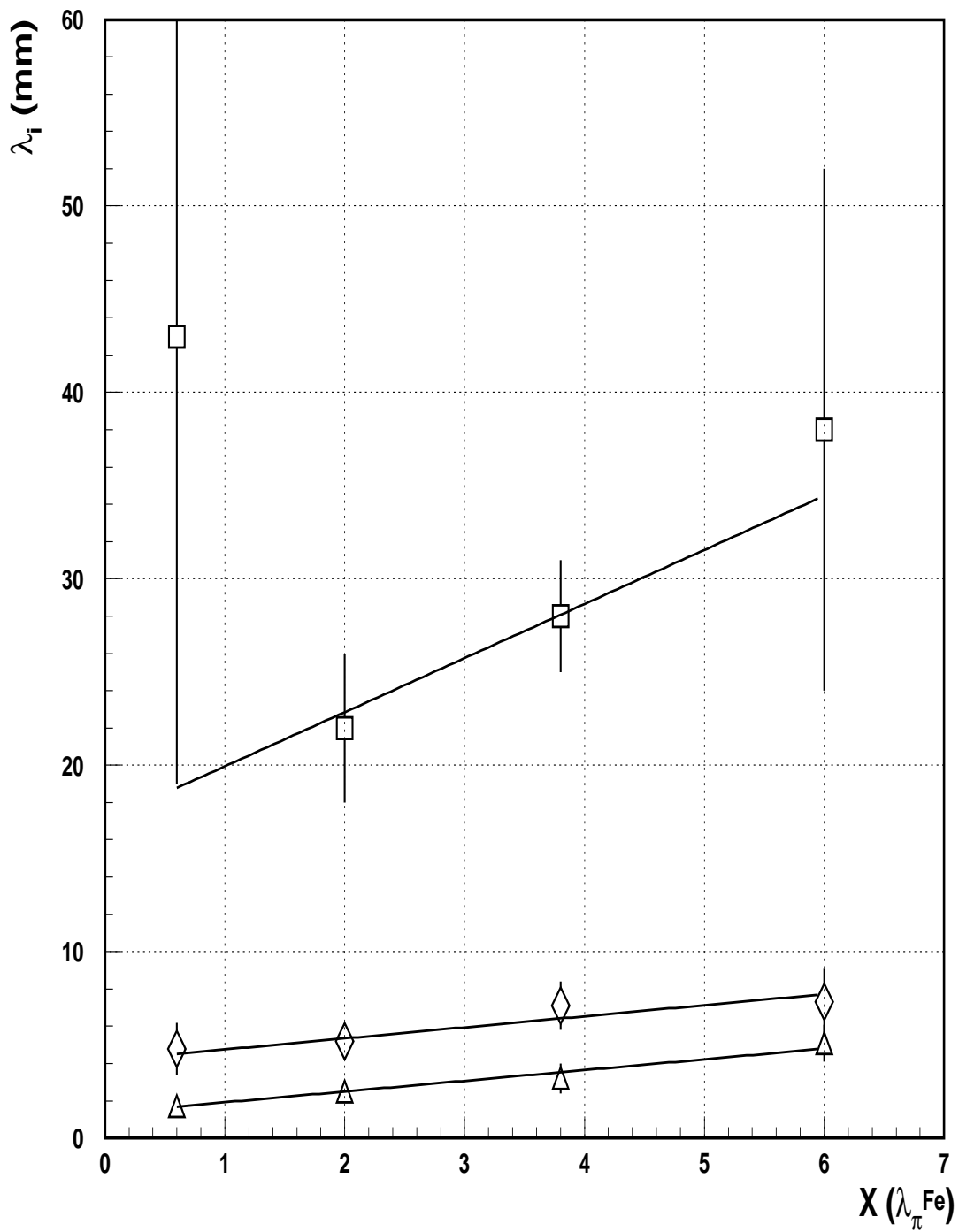


Figure 8:  $X$  dependences of the parameters  $\lambda_i$ : the triangles are the  $\lambda_1$  parameter, the diamonds are the  $\lambda_2$ , the squares are the  $\lambda_3$ .



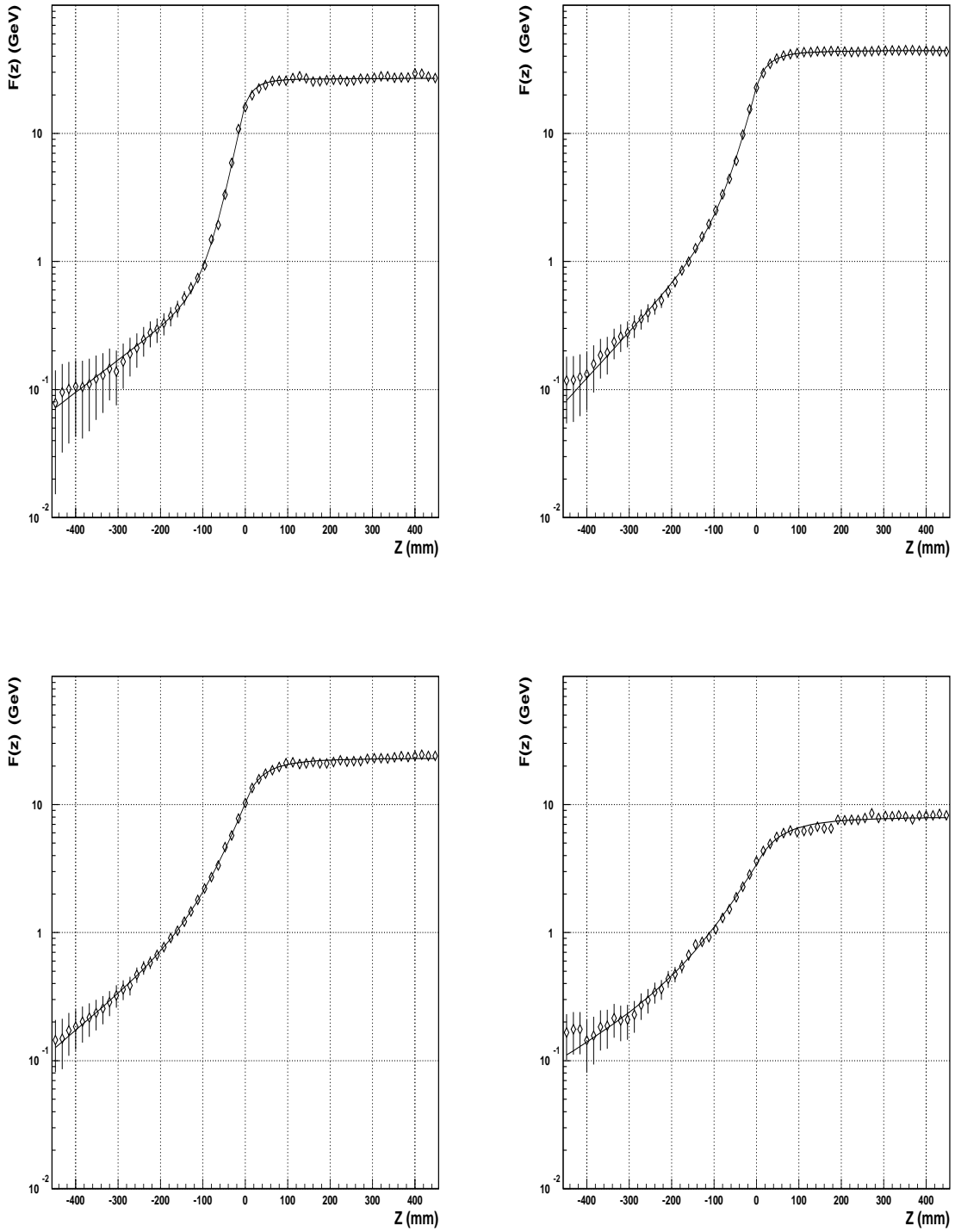


Figure 9: Cumulative functions  $F(z)$  for depth segments 1 – 4 as a function of the  $z$  coordinate: top left is for depth segment 1, top right is for depth segment 2, bottom left is for depth segment 3, bottom right is for depth segment 4. Statistical and systematic errors, summed in quadrature, are shown. Curves are fits of equations (16) and (17) to the data.

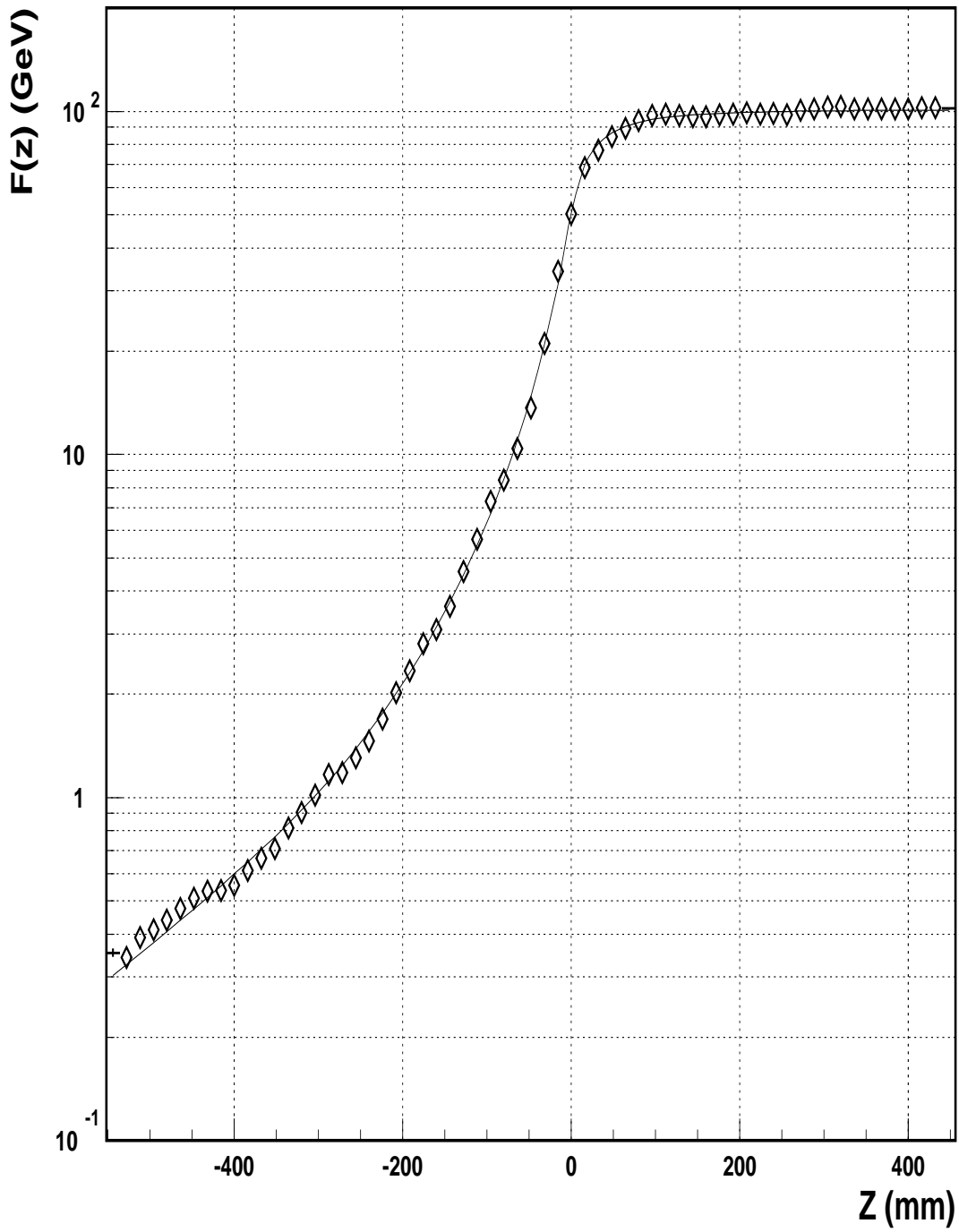


Figure 10: The cumulative function  $F(z)$  for the entire calorimeter as a function of the  $z$  coordinate. Only statistical errors are shown. Curves are fits of equations (16) and (17) to the data.

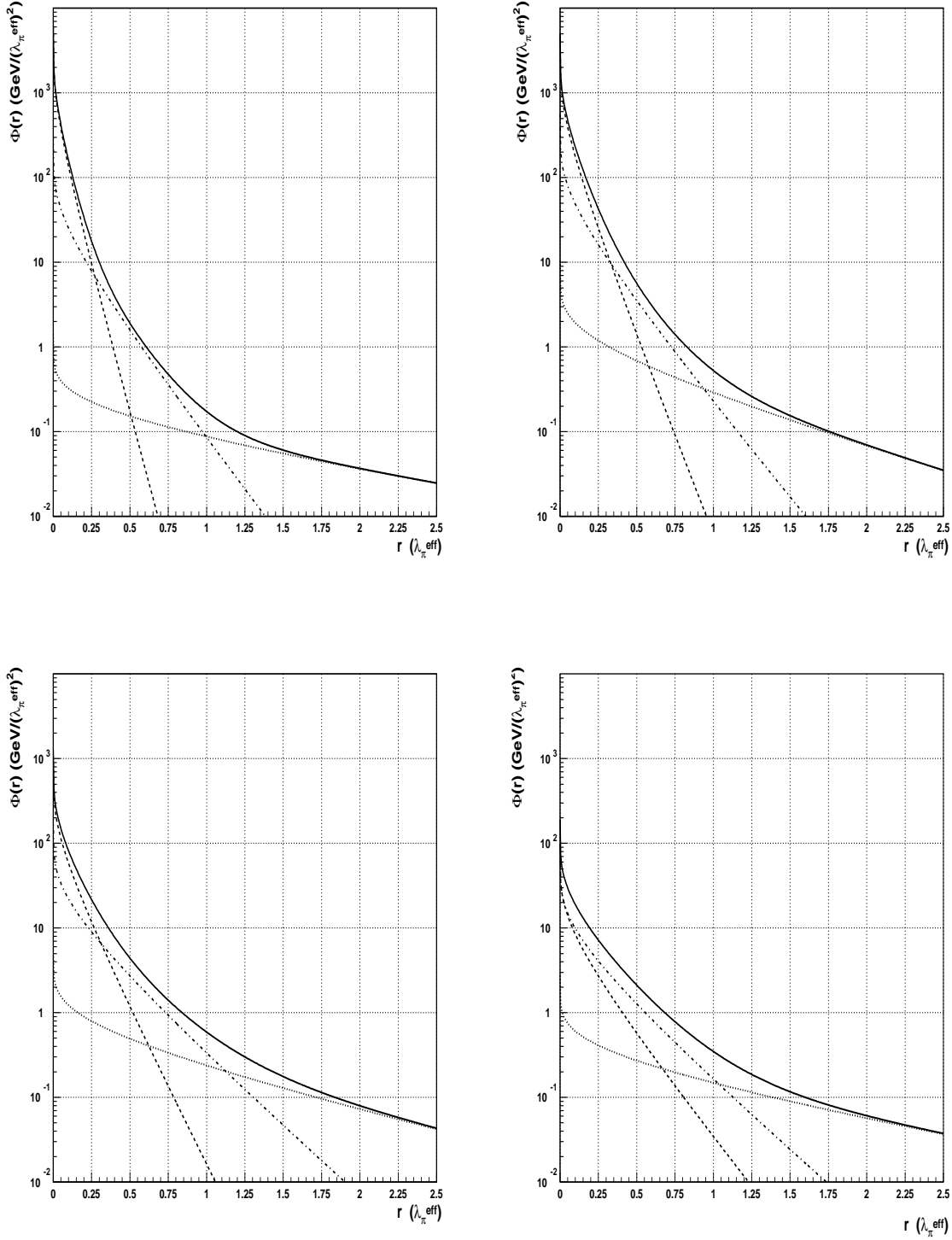


Figure 11: Radial energy density,  $\Phi(r)$ , as a function of  $r$  for Tile calorimeter for depth segments 1 – 4: top left is for depth segment 1, top right is for depth segment 2, bottom left is for depth segment 3, bottom right is for depth segment 4. The solid lines are the energy densities  $\Phi(r)$ , the dashed lines are the contribution from the first term from equation (11), the dash-dotted lines are the contribution from the second term, the dotted lines are the contribution from the third term.

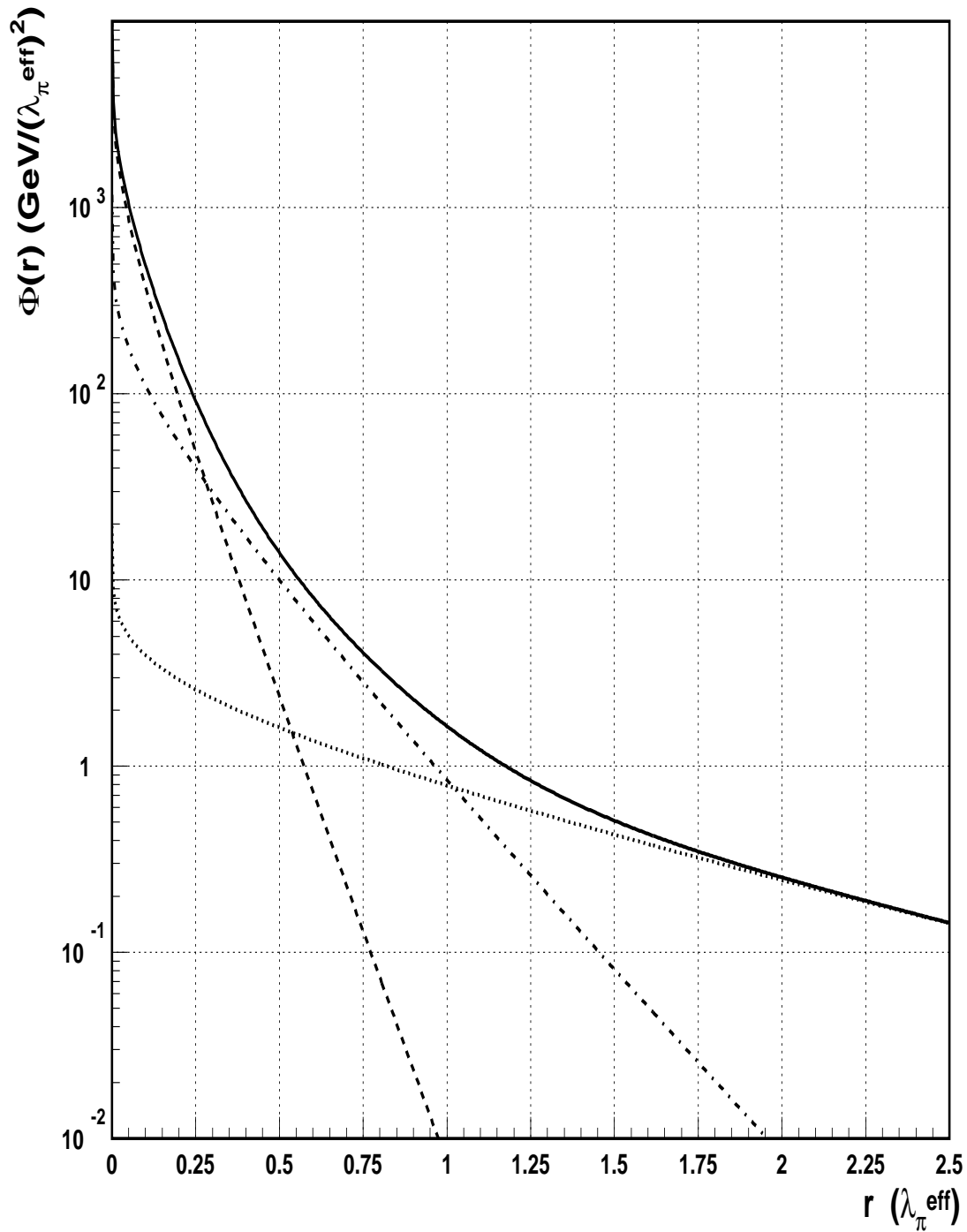


Figure 12: The radial energy density as a function of  $r$  (in units of  $\lambda_{\pi}^{eff}$ ) for Tile calorimeter (the solid line), the contribution to  $\Phi(r)$  from the first term in equation (11) (the dashed line), the contribution to  $\Phi(r)$  from the second term (the dash-dotted line), the contribution to  $\Phi(r)$  from the third term (the dotted line).

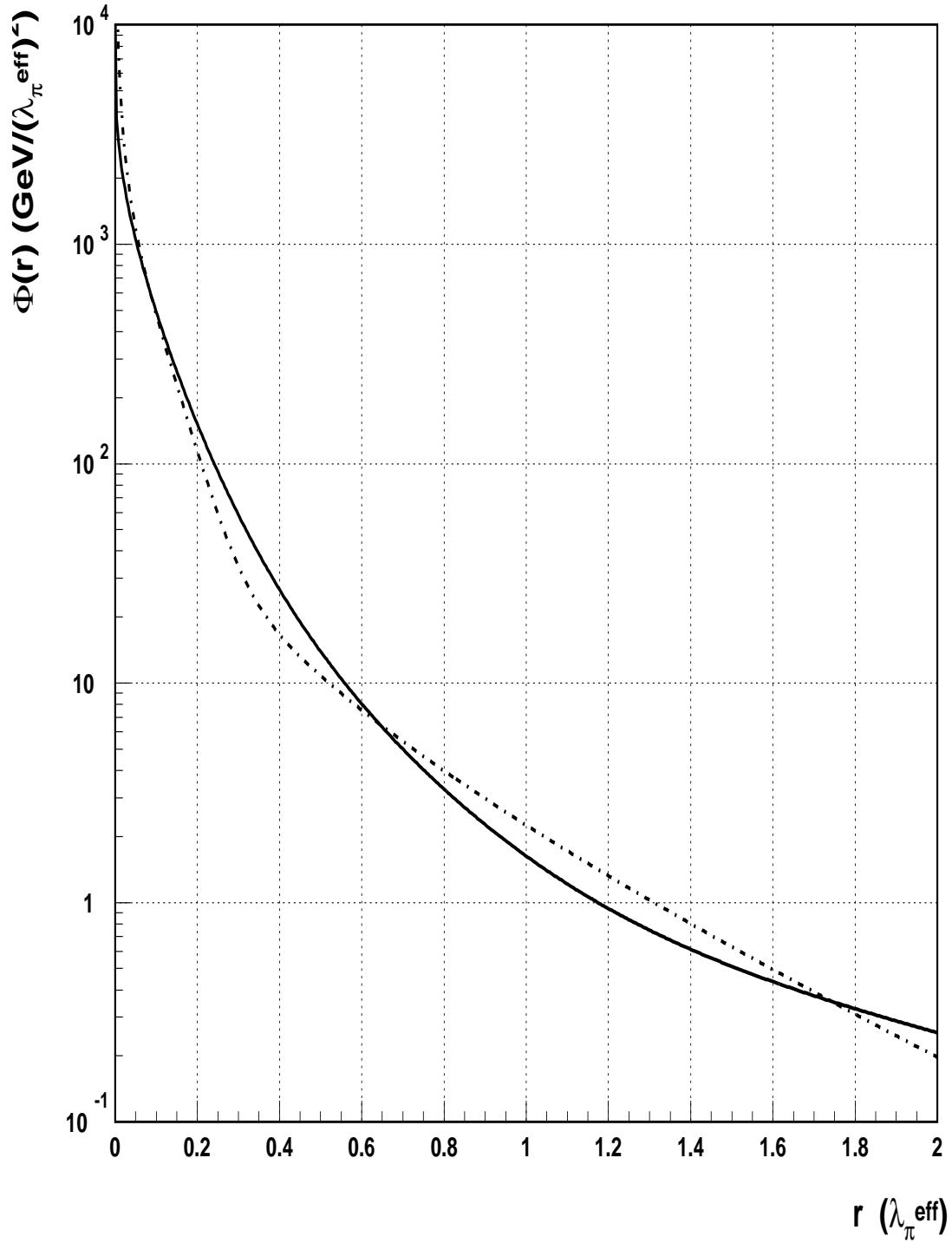


Figure 13: Comparison of the radial energy densities as a function of  $r$  (in units of  $\lambda_{\pi}^{eff}$ ) for Tile calorimeter (the solid line) and lead-scintillating fiber calorimeter (the dash-dotted line).

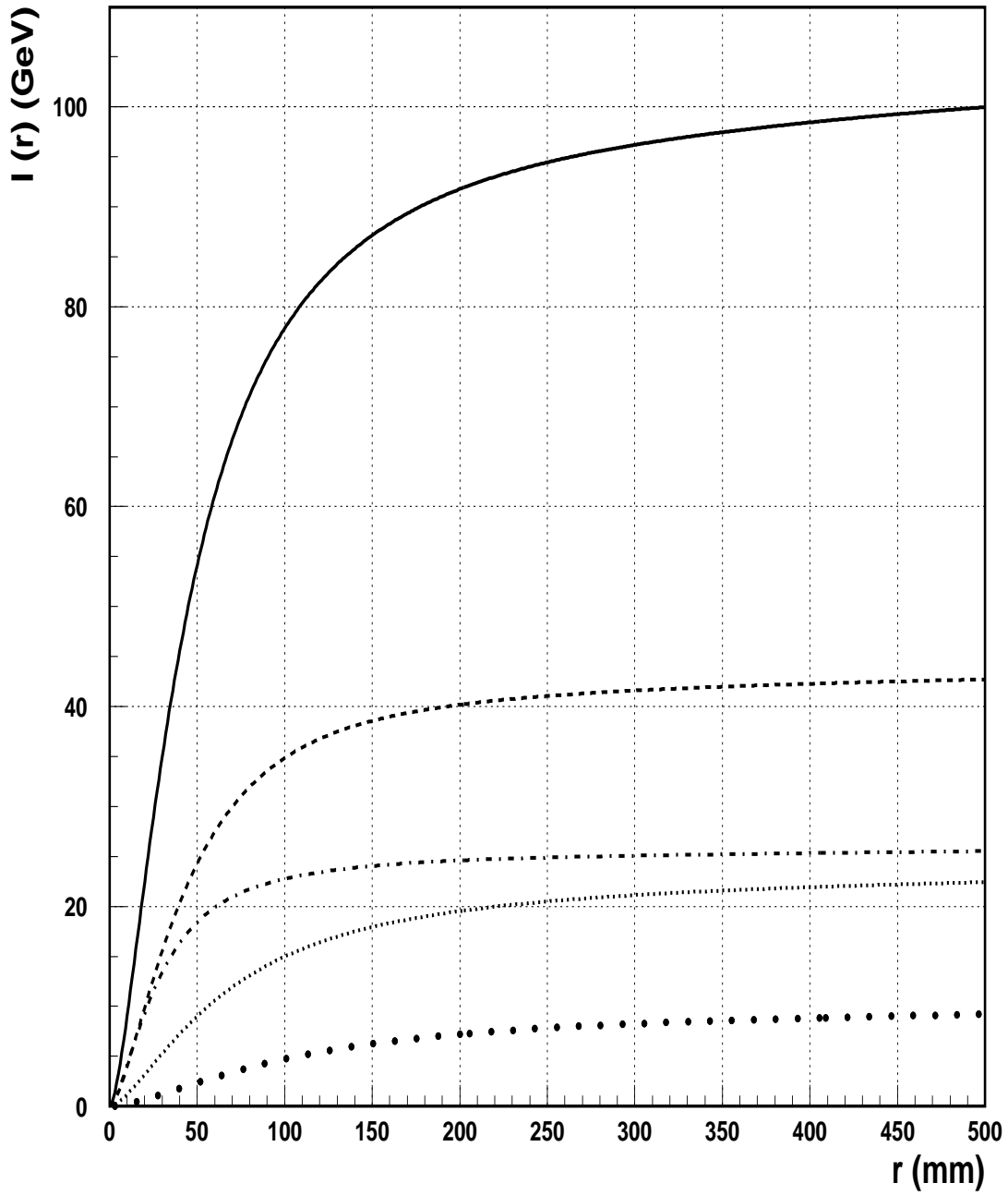


Figure 14: Containment of shower  $I(r)$  (the solid line) as a function of radius for the entire Tile calorimeter. The dash-dotted line is the contribution from the first depth segment, the dashed line is the contribution from the second depth segment, the thin dotted line is the contribution from the third depth segment, the thick dotted line is the contribution from the fourth depth segment.

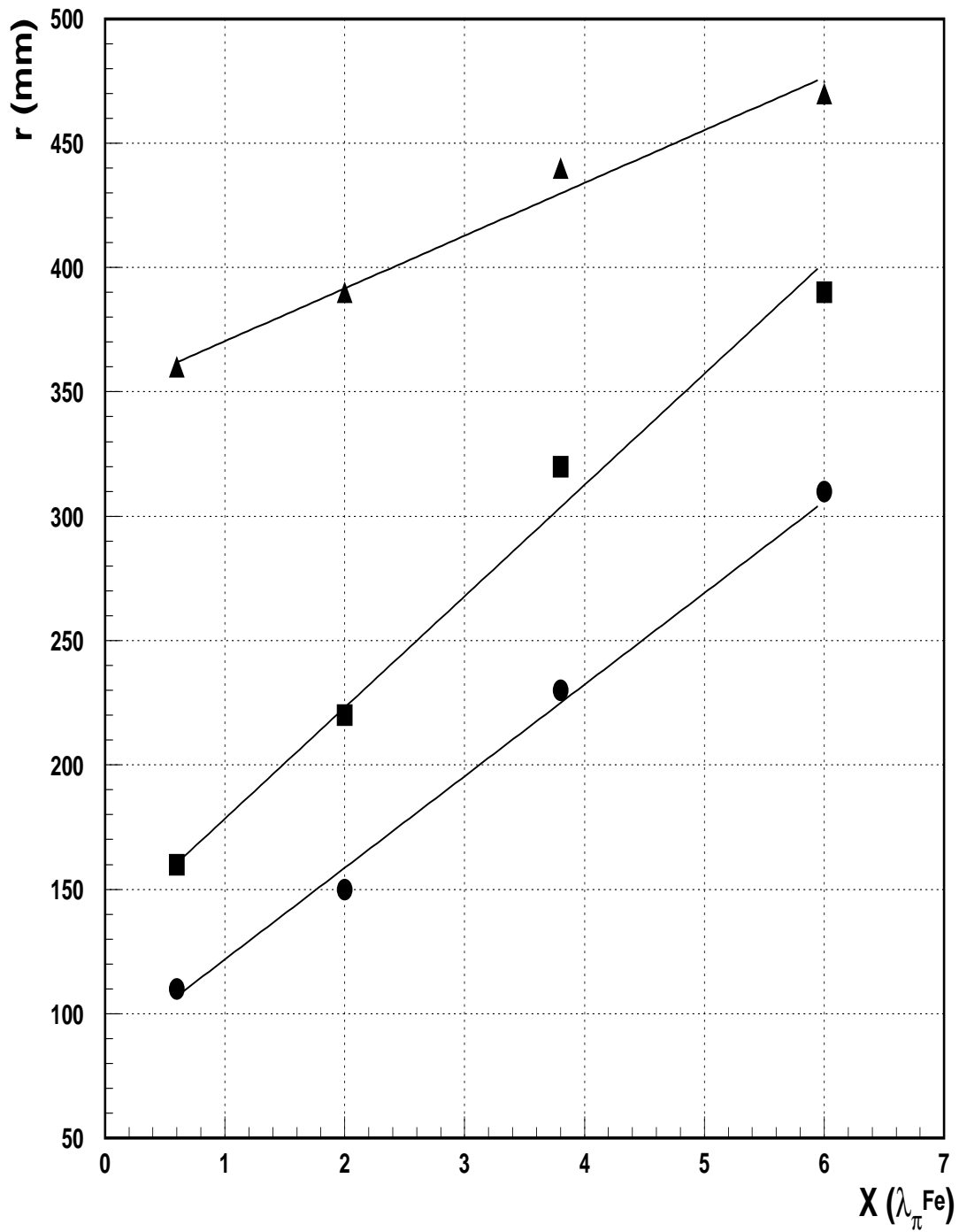


Figure 15: The radii of cylinders for the given shower containment as a function of depths: the black circles are 90% of containment, the black squares are 95%, the black triangles are 99%.

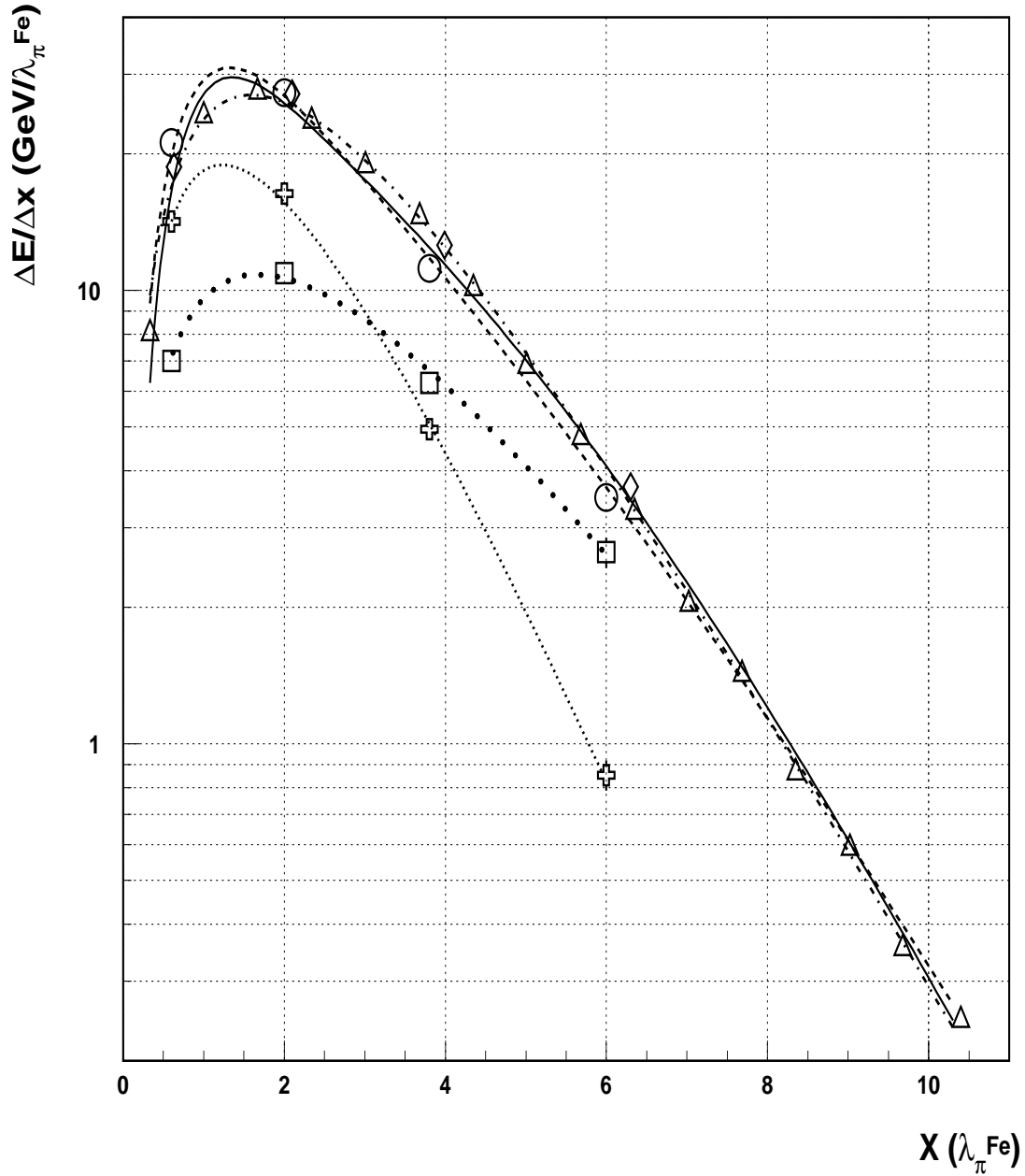


Figure 16: The longitudinal profile (circles) of the hadronic shower at 100 GeV as a function of the longitudinal coordinate  $x$  in units of  $\lambda_{\pi}^{Fe}$ . Open triangles are data from the calorimeter of Ref. [27], diamonds are the Monte Carlo (GEANT-FLUKA) predictions. The dash-dotted line is the fit by function (23), the solid line is calculated with function (24) with parameters from Ref. [27], the dashed line is calculated with function (24) with parameters from Ref. [5]. The electromagnetic and hadronic components of the shower (crosses and squares), together with their fits using (23), are discussed in Section 9.



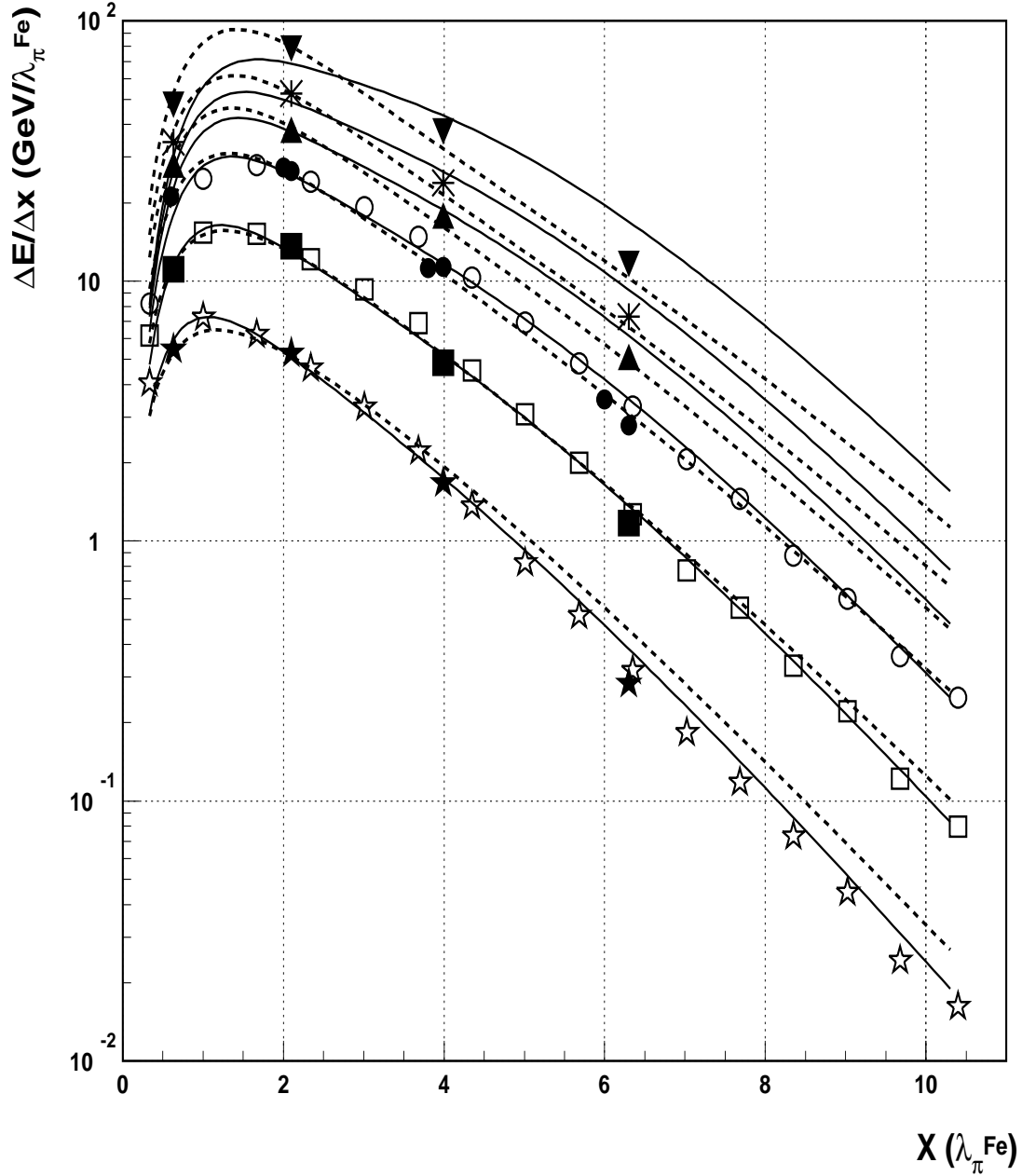


Figure 17: Longitudinal profiles of the hadronic showers from 20 GeV (open stars), 50 GeV (open squares) and 100 GeV (open circles) pions as a function of the longitudinal coordinate  $x$  in units of  $\lambda_I$  for a conventional iron-scintillator calorimeter [27] and of 20 GeV (black stars), 50 GeV (black squares), 100 GeV (black circles), 150 GeV (black up triangles), 200 GeV (asterisks), 300 GeV (black down triangles) for pions at  $20^\circ$  and of 100 GeV (black circles) for pions at  $10^\circ$  for Tile iron-scintillator calorimeter. The solid lines are calculated with function (24) with parameters from [27]. The dashed lines are calculated with function (24) with parameters from [5].

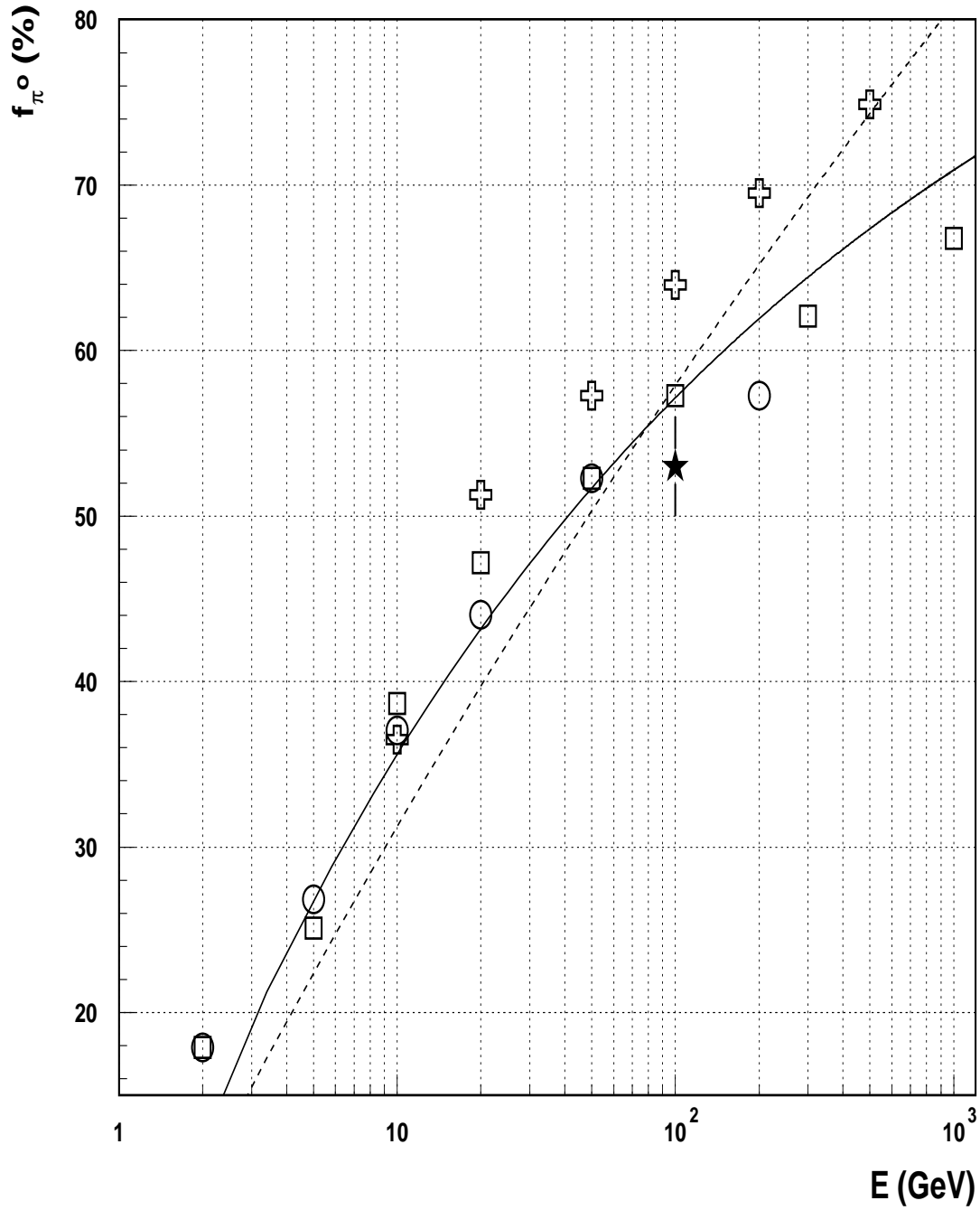


Figure 18: The fraction  $f_{\pi^0}$  in hadronic showers versus the beam energy. The star is our data, the solid curve is the Groom parametrization, the dashed curve is the Wigmans parametrization, squares are the GEANT-CALOR predictions, circles are the GEANT-GHEISHA predictions and crosses are the CALOR predictions.

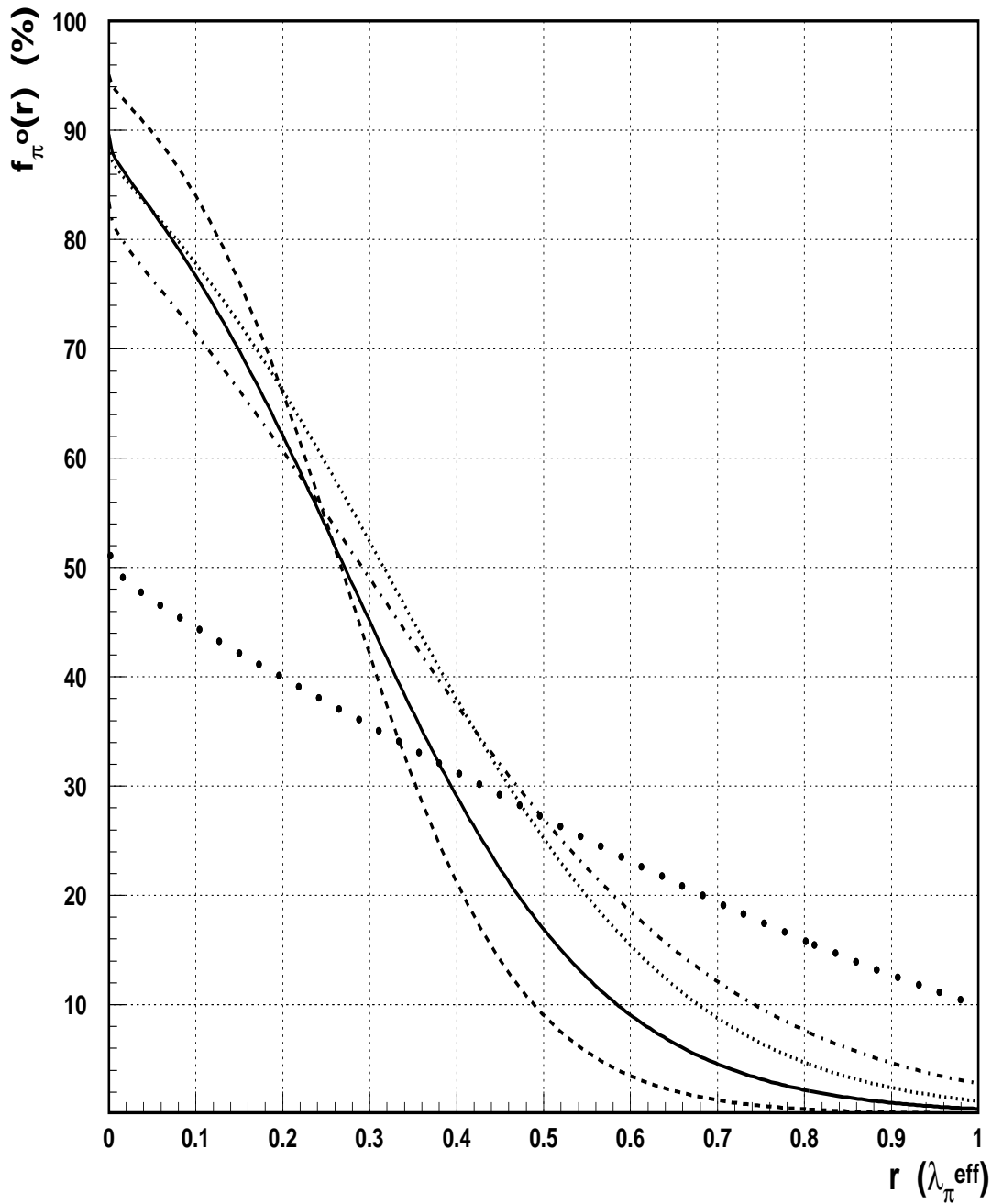


Figure 19: The  $f_{\pi^0}$  fractions of hadronic showers as a function of radius. The solid line is the  $f_{\pi^0}(r)$  for the entire Tile calorimeter. The dash-dotted line is the  $f_{\pi^0}(r)$  for the first depth segment, the dashed line is the  $f_{\pi^0}(r)$  for the second depth segment, the thin dotted line is the  $f_{\pi^0}(r)$  for the third depth segment, the thick dotted line is the  $f_{\pi^0}(r)$  for the fourth depth segment.

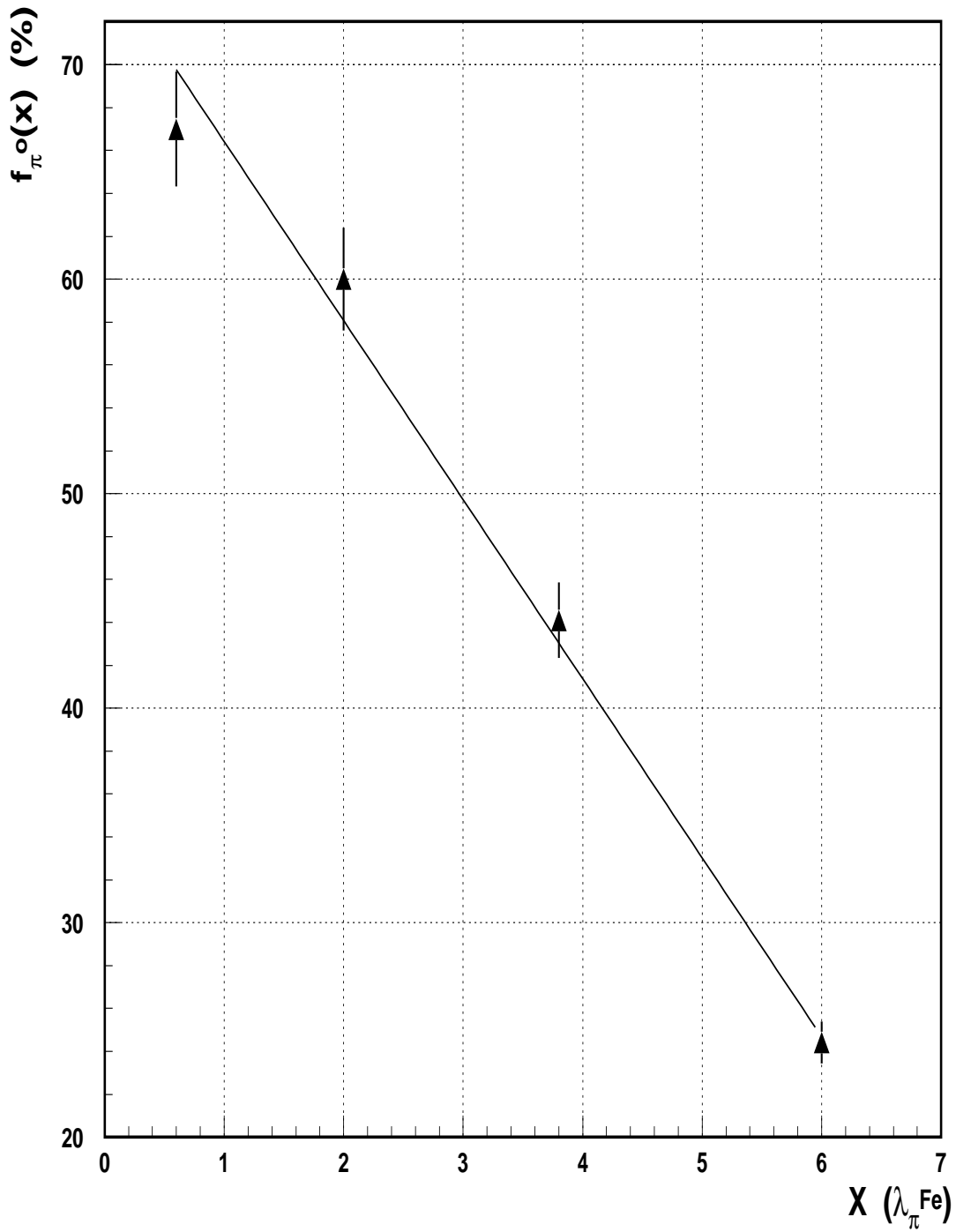


Figure 20: The  $f_{\pi^0}(x)$  fractions of hadronic showers as a function of  $x$ .